











Supermassive black holes are growing slowly by $z \sim 5$

Samuel Lai,^{1,2}       Christopher A. Onken,^{1,3}  Christian Wolf,^{1,3}  Fuyan Bian,⁴  and Xiaohui Fan⁵ 

¹Research School of Astronomy and Astrophysics, Australian National University, Canberra, ACT 2611, Australia

²Commonwealth Scientific and Industrial Research Organisation (CSIRO), Space & Astronomy, P. O. Box 1130, Bentley, WA 6102, Australia

³Centre for Gravitational Astrophysics, Research Schools of Physics, and Astronomy and Astrophysics, Australian National University, Canberra, ACT 2611, Australia

⁴European Southern Observatory, Alonso de Córdova 3107, Casilla 19001, Vitacura, Santiago 19, Chile

⁵Steward Observatory, University of Arizona, 933 N Cherry Ave, Tucson, AZ 85721, USA

Accepted XXX. Received YYY; in original form ZZZ

ABSTRACT

We investigate the black hole mass function at $z \sim 5$ using XQz5, our recent sample of the most luminous quasars between the redshifts $4.5 < z < 5.3$. We include 72 quasars with black hole masses estimated from velocity-broadened emission-line measurements and single-epoch virial prescriptions in the footprint of a highly complete parent survey. The sample mean Eddington ratio and standard deviation is $\log \lambda \approx -0.20 \pm 0.24$. The completeness-corrected mass function is modelled as a double power-law, and we constrain its evolution across redshift assuming accretion-dominated mass growth. We estimate the evolution of the mass function from $z = 5 - 4$, presenting joint constraints on accretion properties through a measured dimensionless e-folding parameter, $k_{\text{ef}} \equiv \langle \lambda \rangle U(1 - \epsilon)/\epsilon = 1.79 \pm 0.06$, where $\langle \lambda \rangle$ is the mean Eddington ratio, U is the duty cycle, and ϵ is the radiative efficiency. If these supermassive black holes were to form from seeds smaller than $10^8 M_{\odot}$, the growth rate must have been considerably faster at $z \gg 5$ than observed from $z = 5 - 4$. A growth rate exceeding $3\times$ the observed rate would reduce the initial heavy seed mass to $10^{5-6} M_{\odot}$, aligning with supermassive star and/or direct collapse seed masses. Stellar mass ($10^2 M_{\odot}$) black hole seeds would require $\gtrsim 4.5\times$ the observed growth rate at $z \gg 5$ to reproduce the measured active black hole mass function. A possible pathway to produce the most extreme quasars is radiatively inefficient accretion flow, suggesting black holes with low angular momentum or photon trapping in supercritically accreting thick discs.

Key words: galaxies: active – galaxies: high-redshift – quasars: supermassive black holes – quasars: emission lines

1 INTRODUCTION

The radiative output of accreting supermassive black holes (SMBHs), which reside in the centres of massive galaxies, is powered by gravitational energy associated with infalling material within the central potential well (e.g. Rees 1984), allowing them to outshine their hosts by orders of magnitude. The extreme luminosities reached by these systems enable them to be observed across cosmological distances, up to $z \sim 7.5$ (e.g., Bañados et al. 2018; Yang et al. 2020; Wang et al. 2021), when the age of the Universe was less than 700 Myr. It is now widely believed that these SMBHs play an important role in regulating host galaxy evolution (see review by Kormendy & Ho 2013), as evidenced by strong correlations between SMBH mass and velocity dispersion (e.g. Magorrian et al. 1998; Ferrarese & Merritt 2000; Gebhardt et al. 2000; Merritt & Ferrarese 2001; Kormendy et al. 2011), bulge mass (e.g. Kormendy & Richstone 1995; Marconi & Hunt 2003; Häring & Rix 2004; Peng et al. 2006; Greene et al. 2010) or total stellar mass (e.g. Cisternas et al. 2011; Reines & Volonteri 2015; Davis et al. 2019; Ding et al. 2020; Smethurst et al. 2023). These tight relations leave little doubt of the existence of feedback mechanisms controlling the host galaxy and SMBH co-evolution (see review by Fabian 2012). Understanding this co-evolution would aid

in the development of a coherent model of galaxy formation and evolution.

In the study of host galaxy and SMBH co-evolution, the black hole mass is an important parameter that is correlated with other galactic properties. However, the best estimates of SMBH mass suggest that the most massive of them are $\gtrsim 10^9 M_{\odot}$ even at early cosmic times, raising questions about the SMBH cosmic mass assembly and the size of black hole seeds (see review by Volonteri et al. 2021). Accretion-dominated mass assembly implies exponential growth with an e-folding time of $450\lambda^{-1}\epsilon(1 - \epsilon)^{-1}$ Myr, where ϵ is the radiative efficiency and λ is the Eddington ratio, $L_{\text{bol}}/L_{\text{edd}}$, with $L_{\text{edd}} = 1.26 \times 10^{38} M_{\text{BH}}/M_{\odot} \text{ erg s}^{-1}$. In order to grow $10^9 M_{\odot}$ black holes within 1 Gyr through accretion, $> 10^2 M_{\odot}$ black hole seeds would be required by 300 Myr ($z \sim 14$), assuming uninterrupted Eddington accretion with the fiducial $\epsilon = 0.1$ radiative efficiency based on the Soltan argument (Soltan 1982; Yu & Tremaine 2002). Other than accretion, black hole mergers also contribute to the evolution of black hole mass. Large-scale hydrodynamical simulations suggest that the role of mergers in the total SMBH mass budget is secondary to growth by accretion (e.g. Dubois et al. 2014; Kulier et al. 2015; Martin et al. 2018). However, at late times when galaxies are comparatively gas-poor, the merger contribution to the total mass budget can increase, especially for the highest mass black holes (e.g. Shankar et al. 2013; Dubois et al. 2014; Kulier et al. 2015). The role

* E-mail: samuel.lai@anu.edu.au

of mergers at high-redshift may be illuminated by the next-generation of gravitational wave interferometers which will extend the redshift horizon and significantly improve the sensitivity to probe mergers of intermediate-mass black holes (Punturo et al. 2010; Amaro-Seoane et al. 2017; Reitze et al. 2019).

In order to explain the observed high-redshift black hole masses, SMBHs must have formed and grown rapidly (e.g. Volonteri & Bellovary 2012). Proposed black hole seeding mechanisms in the early Universe include gravitational collapse of Population III stars (e.g. Madau & Rees 2001; Volonteri et al. 2003), runaway merging (e.g. Portegies Zwart et al. 2004; Seth et al. 2008; Devecchi & Volonteri 2009), or direct collapse (e.g. Loeb & Rasio 1994; Wise et al. 2008; Regan & Haehnelt 2009). Phases of super-Eddington growth or radiatively inefficient accretion can also help alleviate constraints on heavy black hole seeds (e.g. Madau et al. 2014; Inayoshi et al. 2016; Lupi et al. 2016). This can be achieved through counter-alignment of the angular momentum vectors of the accretion disc and black hole or uncorrelated mass injection (e.g. King & Pringle 2006; Zubovas & King 2021).

Observations of high-redshift SMBHs and reliable black hole mass measurements are necessary to study quasar demographics and cosmic mass assembly. Large sky surveys have improved sample statistics across a wide range of luminosities and redshifts (e.g. Shen et al. 2011; Flesch 2015; Rakshit et al. 2020; Wu & Shen 2022), while focused surveys of the ultraluminous quasar subset have directly probed the most massive black hole population and provided stringent constraints on their evolution (e.g. Trakhtenbrot et al. 2011; López et al. 2016; Bischetti et al. 2017; Schindler et al. 2017; Onken et al. 2022; Cristiani et al. 2023; D’Odorico et al. 2023).

The most direct quasar demographic studies are based on the quasar luminosity function which has been used to measure active galactic nuclei (AGN) populations and their evolution across a wide range of redshifts (e.g. Willott et al. 2010a; Jiang et al. 2016; Yang et al. 2016; Akiyama et al. 2018; Matsuoka et al. 2018; McGreer et al. 2018; Niida et al. 2020; Onken et al. 2022; Matsuoka et al. 2023). Demographic analyses on high-redshift quasars become increasingly difficult due to declining quasar spatial densities, requiring deeper wide-area surveys (e.g. Matsuoka et al. 2016, 2023; Schindler et al. 2023). Naturally, the faint-end of the luminosity function suffers from incompleteness and the bright-end is affected by small number statistics ($\lesssim 1 \text{ Gpc}^{-3}$). Another key limitation is the relatively unknown fraction of obscured quasars which can be reddened beyond the typical optical and ultraviolet quasar selection criteria (Ni et al. 2020), requiring multiwavelength observations for candidate selection and spectroscopic identification.

However, the luminosity function does not directly reflect the mass assembly history, which is more clearly measured by the black hole mass. Follow-up spectroscopic observations are used to estimate black hole masses from quasars identified in large sky surveys using “single-epoch virial mass estimators” (e.g. Vestergaard & Peterson 2006; Shen 2013), which are based on empirical relationships from reverberation mapping experiments (e.g. Kaspi et al. 2000, 2005). Black hole mass estimates of luminosity-selected samples have enabled measurements of the black hole mass function and its cosmic evolution (e.g. Greene & Ho 2005; Vestergaard & Osmer 2009; Shankar et al. 2009; Willott et al. 2010b; Kelly & Merloni 2012; Kelly & Shen 2013; Schulze et al. 2015; Ananna et al. 2022; He et al. 2024). Translating the flux-limited selection function to the black hole mass function requires assumptions of the Eddington ratio distribution weighted by the quasar duty cycle. Forward-modelling approaches have been developed to better account for uncertainties and biases in measured quantities (e.g. Kelly et al. 2009; Schulze & Wisotzki

2010; Schulze et al. 2015; Wu et al. 2022). One can also constrain a model-independent active black hole mass function directly from observables using volume-weighted binned quasar abundances (i.e. $1/V_{\text{max}}$ approach; Schmidt 1968), but the result does not necessarily reflect the intrinsic underlying black hole population.

The work by He et al. (2024), hereafter H24, is a study of the $z \sim 4$ black hole mass function based on a sample of 52 quasars from the Hyper Suprime-Cam Subaru Strategic Program and 1462 quasars from the Sloan Digital Sky Survey data release 7 quasar catalog (Shen et al. 2011). By identifying quasar candidates as faint as $i\text{-mag} = 23.2$ using $g\text{-band}$ drop-out colours, H24 presents constraints on the black hole mass function down to $\log M_{\text{BH}}/M_{\odot} \sim 7.5$. We use the low-mass abundance constraints of H24 in the construction of the $z \sim 5$ mass function.

In this work, we study the evolution of the active black hole mass function from $z \sim 5$ to $z \sim 4$ and discuss how the measured growth rate extrapolates to higher redshifts. Using a spectroscopic follow-up of the most luminous and complete sample of quasars between $4.5 < z < 5.3$ (XQz5; Lai et al. 2024) supplemented by literature quasars in the same survey footprint (referred to hereafter as XQz5+), we present measurements of the active black hole mass function at $z \sim 5$. We measure the mass evolution observed between the $z \sim 5$ and $z \sim 4$ mass functions, as well as within the XQz5+ sample itself, which spans ~ 240 Myr of cosmic time. We discuss the implications of our result on the quasar duty cycle, the spin-dependent radiative efficiency, and the size of black hole seeds at earlier cosmic epochs.

The content of this paper is organised as follows: in Section 2, we describe our method, beginning with a description of the $z \sim 5$ quasar sample and its parent survey. We then discuss our approach to measuring and modelling the black hole mass distribution function with the completeness correction of the sample. In Section 3, we apply our method to measure the black hole mass function for $z \sim 5$ and measure its redshift evolution with literature mass functions at different redshifts. We also discuss measuring the mass evolution within the $z \sim 5$ sample using a Monte Carlo mock universe model. We present a summary and conclusion in Section 4. For this study, we adopt a standard flat Λ CDM cosmology with $H_0 = 70 \text{ km s}^{-1} \text{ Mpc}^{-1}$ and $(\Omega_m, \Omega_\Lambda) = (0.3, 0.7)$.

2 METHOD

The sample used in our analysis, XQz5 (Lai et al. 2024), is based on a survey of southern quasars with unprecedented completeness (Onken et al. 2022, hereafter O22). From this parent survey, we construct a spectral atlas of ultraluminous $z \sim 5$ quasars composed of optical and near-infrared spectroscopic follow-up observations of the brightest 83 quasars in the O22 survey between the redshift range $4.5 < z < 5.3$. The spectroscopic follow-up was performed with the following instruments: SOAR/TripleSpec4.1, VLT/X-shooter, and ANU2.3m/WiFeS, and the reduced data have been made publicly available. A full description of the observations and the data reduction was published by Lai et al. (2024).

2.1 Sample completeness

The O22 parent sample utilises the SkyMapper Southern Survey Data Release 3 (SMSS DR3; Wolf et al. 2018; Onken et al. 2019) in combination with precision astrometry from Gaia DR2/eDR3 as well as infrared photometric surveys from Two Micron All-Sky Survey (2MASS; Skrutskie et al. 2006), the VISTA Hemisphere Survey (VHS; McMahan et al. 2013) DR6, VISTA Kilo-Degree Infrared

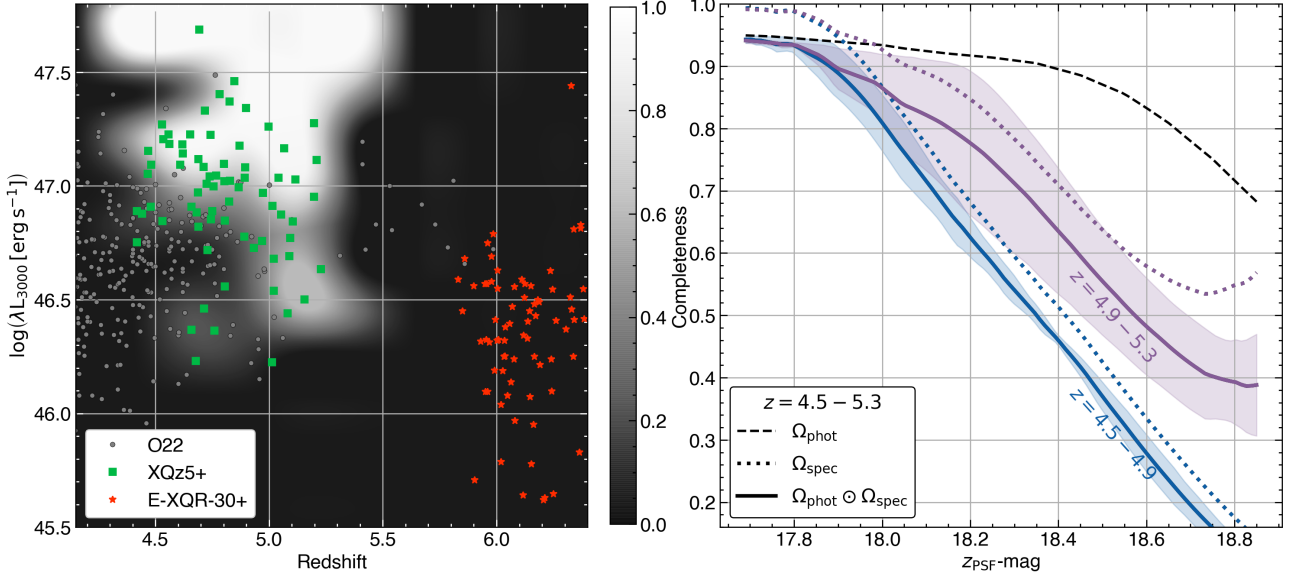


Figure 1. (Left:) Completeness function on a 2-D grid of luminosity and redshift, where the photometric and spectroscopic completeness is mapped onto the parameter space in grayscale. The L_{3000} monochromatic luminosity is estimated from the H -band magnitude as described in O22. Each quasar in the O22 parent sample is shown with a gray point, and the quasars with spectroscopic follow-up that we use in the $z \sim 5$ analysis are overplotted as green squares. We estimate the completeness of the spectroscopic follow-up down to $z = 5.4$, where the parent sample is assumed to be incomplete. We show E-XQR-30+ with red stars as a high-redshift comparison sample. (Right:) Median completeness as a function of $z_{\text{PSF}}\text{-mag}$ estimated between the redshift range $4.5 < z < 5.3$, with the spectroscopic completeness binned into $4.5 < z < 4.9$ and $4.9 < z < 5.3$. The total completeness is shown in solid lines with the median absolute deviation across redshifts represented as sheaths. The photometric and spectroscopic completeness, Ω_{phot} and Ω_{spec} , are shown with the dashed and dotted lines respectively, where the photometric completeness is defined for the entire redshift range.

Galaxy Survey (VIKING; Edge et al. 2013) DR5, AllWISE (Wright et al. 2010; Cutri et al. 2013), and CatWISE2020 (Marocco et al. 2021). The full survey covers $14,486 \text{ deg}^2$ of the sky, including all known quasars in the search area as listed in the MilliQuas v7.1 update (Flesch 2015) and 126 newly identified luminous ($M_{1450} < -27 \text{ mag}$) quasars. The magnitude-dependent completeness, defined in Figure 4 of O22 as a function of the SMSS z -band, declines from 95% at $z_{\text{PSF}} = 17.5$ and 90% at $z_{\text{PSF}} = 18.4 \text{ mag}$ to 78% at $z_{\text{PSF}} = 18.7 \text{ mag}$. The survey is assumed to be complete up to $z = 5.4$, where the redshift constraints are imposed by the absence of signal in the Gaia G -passband from which astrometric measurements are made (O22).

The full completeness correction in our study, $\Omega(L, z)$, is the Hadamard product of the 1-D magnitude-dependent completeness of O22 converted to luminosity, $\Omega_{\text{phot}}(L, z)$, and the completeness of the spectroscopic follow-up, $\Omega_{\text{spec}}(L, z)$, described by

$$\Omega(L, z) = \Omega_{\text{phot}}(L, z) \odot \Omega_{\text{spec}}(L, z), \quad (1)$$

where $\Omega_{\text{spec}}(L, z)$ is estimated in a 2-D grid of luminosity and redshift. In the left panel of Figure 1, we show the 2-D completeness function on a grid of L_{3000} monochromatic luminosity and redshift, where L_{3000} is estimated from a composite spectrum of bright $z = 1-2$ quasars (Selsing et al. 2016) scaled to the H -band magnitude as described in O22. We show the parent sample as grey points and observed sample as green squares. The spectroscopic completeness is determined by the fraction of quasars in O22 that are included in our sample with near-IR spectroscopic follow-up, smoothly interpolated over the grid. We also plot a high-redshift comparison sample as red stars, which is a combination of E-XQR-30 (D’Odorico et al. 2023) augmented by the database of Fan et al. (2023) into a compilation we refer to as E-XQR-30+.

In the right panel of Figure 1, we show the photometric (dashed line), spectroscopic (dotted lines), and full completeness (solid lines)

measured as a function of the z_{PSF} -magnitude between two bins of redshift over $4.5 < z < 5.3$. The spectroscopic completeness, Ω_{spec} , and its uncertainty are measured by the median and median absolute deviation over the redshift range. In the plot, the z_{PSF} range is limited to the region where the spectroscopic completeness is well-behaved, at magnitudes of $z_{\text{PSF}} < 18.85$, approximately corresponding to $\log \lambda L_{3000}/\text{erg s}^{-1} \gtrsim 46.8$ at $z \sim 5$. Our sample is more complete at higher redshifts with the median completeness between the two redshift bins deviating by ~ 0.1 around $z_{\text{PSF}} \sim 18.1$.

Our analysis is primarily focused on the high luminosity ($\log \lambda L_{3000}/\text{erg s}^{-1} \gtrsim 46.8$) quasars between redshifts $4.5 < z < 5.3$, for which we have well-defined completeness. The surveyed sky area contains 55/84 of the XQz5 quasars (majority of which are excluded by sky position), as well as 9 quasars from Trakhtenbrot et al. (2011), hereafter T11, and 8 quasars from López et al. (2016), hereafter XQ100. The final dataset is composed of 72 quasars. The T11 and XQ100 quasars supplement the lower-luminosity and lower-redshift ends of the sample, respectively. These additional quasars are targets within the footprint of O22 which were already observed with spectroscopic follow-up and thus repeat observations were not scheduled for the XQz5 dataset. We adopt the measured black hole masses from the T11 and Lai et al. (2023) analyses, respectively, using the virial estimator and calibration described in Section 2.2. We present all 72 quasars used in our demographic analysis in Table 1 and we refer to the expanded dataset as XQz5+. The monochromatic $\log \lambda L_{3000}/\text{erg s}^{-1}$ luminosity in Table 1 is measured from the near-infrared spectroscopic observations rather than the H -band magnitude. The mean difference and standard deviation is $\Delta \log \lambda L_{3000}/\text{erg s}^{-1} = -0.04 \pm 0.04$. In the following section, we discuss how the completeness correction is used to measure the observed black hole mass distribution function.

Table 1. Properties of quasars in XQz5+ used in the demographic analysis.

ID	RA (J2000)	Dec (J2000)	Redshift	$\log L_{3000}/\text{erg s}^{-1}$	$\log M_{\text{BH}}/M_{\odot}$	$\log L_{\text{bol}}/L_{\text{Edd}}$	Source
000651–620803	1.71502	-62.13430	4.44	46.787 ± 0.029	9.73 ± 0.05	-0.45 ± 0.05	XQ100
001225–484829	3.10424	-48.80830	4.62	47.256 ± 0.019	9.80 ± 0.05	-0.06 ± 0.05	XQz5
001714–100055	4.31113	-10.01536	5.02	46.547 ± 0.023	9.37 ± 0.10	-0.34 ± 0.11	XQz5
002526–014532	6.36181	-1.75905	5.06	47.072 ± 0.036	9.33 ± 0.05	0.23 ± 0.06	XQz5
003525+004002	8.85542	0.66750	4.76	46.380 ± 0.150	8.49 ± 0.44	0.38 ± 0.46	T11
011546–025312	18.94274	-2.88676	5.08	46.505 ± 0.005	9.51 ± 0.07	-0.52 ± 0.07	XQz5
013127–032059	22.86391	-3.34998	5.20	47.108 ± 0.029	9.50 ± 0.10	0.10 ± 0.10	XQz5
013539–212628	23.91370	-21.44118	4.90	47.385 ± 0.011	10.05 ± 0.26	-0.18 ± 0.26	XQz5
014741–030247	26.92301	-3.04659	4.80	47.199 ± 0.007	10.41 ± 0.04	-0.72 ± 0.04	XQz5
015618–044139	29.07906	-4.69444	4.93	46.557 ± 0.024	9.28 ± 0.11	-0.24 ± 0.11	XQz5
020436–252315	31.15277	-25.38757	4.87	46.965 ± 0.016	9.24 ± 0.04	0.21 ± 0.05	XQz5
021043–001818	32.67984	-0.30510	4.71	46.040 ± 0.080	9.09 ± 0.40	-0.56 ± 0.41	T11
022112–034252	35.30259	-3.71447	5.02	46.535 ± 0.044	9.05 ± 0.17	-0.03 ± 0.18	XQz5
022306–470902	35.77812	-47.15069	5.00	47.297 ± 0.018	9.96 ± 0.08	-0.17 ± 0.09	XQz5
023648–114733	39.20236	-11.79268	5.20	46.890 ± 0.013	9.77 ± 0.12	-0.39 ± 0.12	XQz5
030722–494548	46.84538	-49.76336	4.72	47.261 ± 0.019	10.07 ± 0.07	-0.32 ± 0.07	XQ100
033119–074142	52.83191	-7.69525	4.73	46.550 ± 0.040	8.83 ± 0.11	0.21 ± 0.12	T11
033703–254831	54.26273	-25.80878	5.11	46.872 ± 0.025	9.64 ± 0.10	-0.28 ± 0.10	XQz5
040732–281031	61.88725	-28.17531	4.74	46.675 ± 0.010	9.19 ± 0.03	-0.03 ± 0.03	XQz5
040914–275632	62.31198	-27.94248	4.48	46.975 ± 0.040	9.74 ± 0.17	-0.28 ± 0.17	XQz5
044432–292419	71.13547	-29.40534	4.82	46.988 ± 0.010	9.89 ± 0.06	-0.41 ± 0.06	XQz5
045057–265541	72.73904	-26.92817	4.77	47.021 ± 0.027	9.72 ± 0.11	-0.21 ± 0.11	XQz5
045427–050049	73.61643	-5.01375	4.83	47.057 ± 0.016	9.76 ± 0.12	-0.21 ± 0.12	XQz5
051508–431853	78.78722	-43.31493	4.61	47.051 ± 0.028	9.69 ± 0.34	-0.15 ± 0.35	XQz5
052915–352603	82.31632	-35.43436	4.42	46.690 ± 0.018	9.22 ± 0.05	-0.04 ± 0.05	XQ100
071431–645510	108.63081	-64.91962	4.46	47.019 ± 0.012	9.61 ± 0.07	-0.11 ± 0.07	XQ100
072011–675631	110.04869	-67.94215	4.62	47.249 ± 0.023	10.08 ± 0.06	-0.35 ± 0.06	XQz5
091655–251145	139.23200	-25.19607	4.85	47.317 ± 0.012	9.77 ± 0.05	0.04 ± 0.05	XQz5
093032–221207	142.63577	-22.20213	4.89	47.022 ± 0.012	9.90 ± 0.06	-0.40 ± 0.06	XQz5
095500–013006	148.75040	-1.50189	4.42	46.814 ± 0.021	9.65 ± 0.04	-0.35 ± 0.05	XQ100
103623–034318	159.09895	-3.72192	4.53	46.766 ± 0.011	9.46 ± 0.03	-0.20 ± 0.03	XQ100
111054–301129	167.72790	-30.19164	4.78	47.335 ± 0.011	10.29 ± 0.05	-0.47 ± 0.05	XQz5
111520–193506	168.83470	-19.58506	4.66	47.019 ± 0.012	9.71 ± 0.07	-0.21 ± 0.07	XQz5
113522–354838	173.84172	-35.81076	4.97	46.952 ± 0.008	9.67 ± 0.03	-0.23 ± 0.04	XQz5

2.2 Black hole mass function

Constraining the shape and evolution of the black hole mass function is observationally expensive, due to the requirement of collecting samples with high completeness and obtaining high signal-to-noise spectroscopic data, which are necessary for reliable black hole mass measurements. Furthermore, the completeness correction of the black hole mass function, particularly for lower masses, is not as easily ascertained, as the mass on its own is not sufficient to adequately constrain the intrinsic luminosity, and hence the observed source brightness (on which the completeness estimate relies). Nevertheless, the cosmic evolution of the black hole mass function is a key component in the developing picture of supermassive black hole origins and growth mechanisms. Here, we describe the method used in this study to measure and parameterise the observed black hole mass function.

In the XQz5+ sample, black hole masses are estimated from near-infrared spectroscopic observations of the Mg II $\lambda 2799$ broad emission line with the single-epoch virial mass estimator of Shen et al. (2011), which is calibrated to the H β line in a high-luminosity subset of the local AGN reverberation mapping sample. The single-epoch virial mass equation takes the form,

$$\left(\frac{M_{\text{BH, vir}}}{M_{\odot}}\right) = 10^a \left[\frac{L_{3000}}{10^{44} \text{ erg s}^{-1}}\right]^b \left[\frac{\text{FWHM}_{\text{Mg II}}}{1000 \text{ km s}^{-1}}\right]^c, \quad (2)$$

where L_{3000} is the monochromatic luminosity (λL_{λ}) of the quasar continuum model at 3000Å and $\text{FWHM}_{\text{Mg II}}$ is the measured full-width at half-maximum of the Mg II broad line profile. The calibration from Shen et al. (2011) is $(a, b, c) = (6.74, 0.62, 2.00)$. The intrinsic scatter of the H β virial mass estimator is ~ 0.3 dex compared to their reverberation mapping counterparts (Dalla Bontà et al. 2020), while reverberation mapping mass estimates are dispersed around the $M_{\text{BH}} - \sigma_*$ relation (Bennert et al. 2021) with a ~ 0.4 dex scatter. Additionally, Mg II-based mass estimates are calibrated to H β , with a dispersion of 0.1 – 0.2 dex (e.g. Shen & Liu 2012). As such, the expected systematic uncertainty from single-epoch virial mass estimators is ~ 0.5 dex, which is often more significant than the measurement uncertainties propagated from the FWHM and continuum luminosity. A more detailed discussion of the systematic uncertainty inherent in single-epoch virial mass measurements is presented in Lai et al. (2023), a study of 100 luminous quasars between $3.5 < z < 4.5$.

The binned black hole mass function between $z_{\text{min}} < z < z_{\text{max}}$ can be estimated using the $1/V_{\text{max}}$ method (Schmidt 1968; Avni & Bahcall 1980; Page & Carrera 2000),

$$\Phi(M_{\text{BH}}, z) = \frac{1}{\Delta \log M_{\text{BH}}} \sum_{i=1}^{N_{\text{BH}}} \frac{f_{\text{obs}}^{-1}}{\int_{z_{\text{min}}}^{z_{\text{max}}} \Omega(L_i, z) \frac{dV}{dz} dz}, \quad (3)$$

where $f_{\text{obs}} \sim 0.351$ is the sky area coverage of our parent sample, $\Omega(L, z)$ is the 2-D completeness correction from Equation 1, and

Table 1. (Continued)

ID	RA (J2000)	Dec (J2000)	Redshift	$\log L_{3000}/\text{erg s}^{-1}$	$\log M_{\text{BH}}/M_{\odot}$	$\log L_{\text{bol}}/L_{\text{Edd}}$	Source
120441–002149	181.17393	-0.36373	5.09	46.585 ± 0.023	9.73 ± 0.06	-0.66 ± 0.07	XQz5
120523–074232	181.34642	-7.70907	4.69	47.229 ± 0.015	10.04 ± 0.09	-0.33 ± 0.09	XQz5
121402–123548	183.51130	-12.59683	4.75	46.777 ± 0.022	9.66 ± 0.09	-0.40 ± 0.10	XQz5
121921–360933	184.83801	-36.15917	4.80	47.046 ± 0.014	10.21 ± 0.02	-0.67 ± 0.03	XQz5
130031–282931	195.12973	-28.49195	4.71	47.023 ± 0.021	9.58 ± 0.14	-0.07 ± 0.14	XQz5
132853–022441	202.22366	-2.41157	4.66	46.280 ± 0.080	9.08 ± 0.24	-0.31 ± 0.25	T11
134134+014157	205.39250	1.69939	4.69	46.730 ± 0.080	9.82 ± 0.24	-0.60 ± 0.25	T11
140801–275820	212.00757	-27.97228	4.47	47.170 ± 0.057	9.99 ± 0.10	-0.34 ± 0.11	XQz5
142721–050353	216.83984	-5.06477	5.09	46.618 ± 0.015	9.51 ± 0.06	-0.41 ± 0.06	XQz5
151443–325024	228.68260	-32.84022	4.83	47.151 ± 0.025	9.36 ± 0.04	0.28 ± 0.05	XQz5
153241–193032	233.17252	-19.50910	4.69	46.871 ± 0.024	9.35 ± 0.05	0.01 ± 0.05	XQz5
153359–181027	233.49907	-18.17420	5.01	46.870 ± 0.041	9.75 ± 0.13	-0.40 ± 0.14	XQz5
155657–172107	239.23904	-17.35207	4.75	46.901 ± 0.009	9.72 ± 0.08	-0.33 ± 0.08	XQz5
160111–182834	240.29657	-18.47638	5.05	46.981 ± 0.019	9.54 ± 0.10	-0.07 ± 0.10	XQz5
194124–450023	295.35245	-45.00656	5.21	47.158 ± 0.016	9.86 ± 0.07	-0.22 ± 0.08	XQz5
205559–601147	313.99667	-60.19648	4.97	46.961 ± 0.015	9.43 ± 0.12	0.01 ± 0.12	XQz5
205724–003018	314.35062	-0.50522	4.68	46.830 ± 0.080	9.23 ± 0.24	0.09 ± 0.25	T11
211105–015604	317.77335	-1.93449	4.89	47.155 ± 0.013	9.86 ± 0.09	-0.22 ± 0.09	XQz5
211920–772253	319.83676	-77.38142	4.56	46.954 ± 0.011	9.96 ± 0.14	-0.52 ± 0.14	XQz5
215728–360215	329.36758	-36.03752	4.69	47.672 ± 0.001	10.33 ± 0.12	-0.17 ± 0.12	XQz5
220008+001744	330.03607	0.29580	4.80	46.510 ± 0.080	8.82 ± 0.24	0.18 ± 0.25	T11
220158–202627	330.49408	-20.44092	4.74	47.014 ± 0.028	9.65 ± 0.09	-0.15 ± 0.09	XQz5
221111–330245	332.79813	-33.04606	4.65	47.231 ± 0.011	9.72 ± 0.06	-0.00 ± 0.06	XQz5
221644+001348	334.18340	0.23001	5.01	46.377 ± 0.007	9.30 ± 0.04	-0.44 ± 0.04	XQz5
221651–671443	334.21664	-67.24540	4.48	46.838 ± 0.020	9.79 ± 0.07	-0.46 ± 0.08	XQ100
221705–001307	334.27374	-0.21870	4.68	46.280 ± 0.150	8.63 ± 0.44	0.14 ± 0.46	T11
222152–182602	335.47037	-18.43412	4.53	47.302 ± 0.018	9.85 ± 0.10	-0.06 ± 0.10	XQz5
222357–252634	335.99112	-25.44284	4.80	46.942 ± 0.026	9.16 ± 0.16	0.27 ± 0.16	XQz5
222509–001406	336.28827	-0.23523	4.89	46.700 ± 0.040	9.27 ± 0.11	-0.08 ± 0.12	T11
222612–061807	336.55173	-6.30200	5.10	46.516 ± 0.015	9.35 ± 0.05	-0.35 ± 0.05	XQz5
222845–075755	337.18805	-7.96533	5.16	46.323 ± 0.032	8.95 ± 0.07	-0.14 ± 0.08	XQz5
223953–055220	339.97360	-5.87223	4.56	47.197 ± 0.012	9.64 ± 0.05	0.04 ± 0.05	XQ100
230349–063343	345.95496	-6.56195	4.74	47.052 ± 0.014	9.89 ± 0.09	-0.35 ± 0.09	XQz5
230429–313426	346.12454	-31.57416	4.87	47.181 ± 0.013	9.93 ± 0.13	-0.26 ± 0.13	XQz5
232536–055328	351.40268	-5.89114	5.23	46.998 ± 0.015	9.75 ± 0.13	-0.26 ± 0.13	XQz5
232952–200039	352.46988	-20.01085	5.04	47.162 ± 0.011	9.59 ± 0.06	0.06 ± 0.06	XQz5
233435–365708	353.64703	-36.95247	4.72	46.990 ± 0.019	9.51 ± 0.29	-0.04 ± 0.29	XQz5
233505–590103	353.77440	-59.01755	4.53	47.262 ± 0.010	9.84 ± 0.06	-0.09 ± 0.06	XQz5

dV/dz is the differential comoving volume element. Poisson statistical uncertainties are estimated for each point in the binned mass function.

The $1/V_{\text{max}}$ method produces a model-independent and non-parametric estimate of the active black hole mass function. However, we caution that the $1/V_{\text{max}}$ approach does not consider the error function in the virial black hole mass estimates (e.g. Kelly et al. 2009; Shen & Kelly 2012; Schulze et al. 2015). The $1/V_{\text{max}}$ approach is expected to be biased by a wide error distribution, which artificially broadens the mass function leading to a shallower high-mass slope due to the large systematic errors in the virial M_{BH} estimates. The survey selection function is also a function of the quasar luminosity, which does not translate directly to completeness in black hole mass (e.g. Schulze & Wisotzki 2010). Therefore, the black hole mass function derived using $1/V_{\text{max}}$ does not reflect the intrinsic black hole mass function. Numerous other studies have discussed the shortcomings of the $1/V_{\text{max}}$ approach in more detail and developed more rigorous statistical frameworks (e.g. Kelly et al. 2009; Schulze & Wisotzki 2010; Schulze et al. 2015; Wu et al. 2022). Nevertheless, studies of high-redshift quasar demographics where statistics are sparse continue to use the straightforward and repro-

ducible $1/V_{\text{max}}$ approach (Matsuoka et al. 2018; Ananna et al. 2022; Matsuoka et al. 2023), if only as a sanity check to complement other more advanced Bayesian methods (e.g. Wu et al. 2022; H24). In this study, we use the $1/V_{\text{max}}$ approach to study the differential growth between mass functions separated by a measurable evolution, which would be equally transformed by convolution with homoscedastic error distributions. Therefore, if the error function is homoscedastic and redshift invariant, the measured active black hole mass function *evolution* presented in this study would be independent of the high-mass bias caused by a wide error function.

Double power-laws are often used to parameterise black hole luminosity functions (e.g. Yang et al. 2016; Akiyama et al. 2018; Matsuoka et al. 2018; Niida et al. 2020; Onken et al. 2022; Matsuoka et al. 2023), tracing back to earlier studies (Boyle et al. 2000) that observe a flattening of the luminosity function at fainter magnitudes. Motivated by fits to quasar luminosity functions, double power-laws have also been adopted to model black hole mass functions (e.g. Li et al. 2023; H24). Alternatively, Schechter-like functional forms (Aller & Richstone 2002), which resemble galactic stellar mass distributions (e.g. Baldry et al. 2012; Davidzon et al. 2017, and references therein), are also used (e.g. Schulze et al. 2015; Ananna et al. 2022;

H24). If black hole properties trace host galaxy properties, it is expected that the underlying intrinsic distribution would resemble the Schechter function (Cappellari et al. 2015). In comparison to the double power-law, we find that the Schechter model applied to our data enhances low-mass abundances with a faster exponential turnoff at high masses. In this study, we expect the double power-law to be a better fit to the $1/V_{\max}$ binned active mass function due to the enhanced spatial abundances at higher masses (see also Schulze & Wisotzki 2010). Therefore, we choose to parameterise the observed mass function at redshift z as,

$$\Phi_z(M_{\text{BH},z}) = \frac{\Phi(M_{\text{BH}}^*)}{(M_{\text{BH},z}/M_{\text{BH}}^*)^{-(\alpha+1)} + (M_{\text{BH},z}/M_{\text{BH}}^*)^{-(\beta+1)}}, \quad (4)$$

where M_{BH}^* is the turnover black hole mass, (α, β) are the low- and high-mass slopes, and $\Phi(M_{\text{BH}}^*)$ is the normalisation. We translate the observed mass function to other redshifts through the continuity equation described in Section 2.3. We derive model parameters $(M_{\text{BH}}^*, \alpha, \beta)$ from fitting the $1/V_{\max}$ binned mass function.

2.2.1 Eddington ratio distribution

The Eddington ratio is the luminosity of the quasar as a fraction of its Eddington luminosity, defined as $\lambda \equiv L_{\text{bol}}/L_{\text{Edd}}$, where $L_{\text{Edd}} = 1.26 \times 10^{38} (M_{\text{BH}}/M_{\odot}) \text{ erg s}^{-1}$. In this study, we estimate $L_{\text{bol}} = 0.75 \times k_{\text{BC}} \times L_{3000}$ based on a quasar mean spectral energy distribution (SED) ($k_{\text{BC}} = 5.15$; Richards et al. 2006) and a 25% anisotropy correction (Runnoe et al. 2012). We caution that L_{3000} -dependent bolometric correction factors as low as $k_{\text{BC}} \sim 2.5$ for $\log(L_{3000}/\text{erg s}^{-1}) = 47.0$ have been suggested by both empirical studies (Trakhtenbrot & Netzer 2012) and thermal accretion disc models (Netzer 2019), which primarily cover the “big blue bump” of the quasar SED (Shields 1978). Bolometric corrections to the hard X-ray component are also found to be correlated with the Eddington ratio with differences of an order of magnitude (Vasudevan & Fabian 2007; Vasudevan et al. 2009), while optical bolometric corrections show no strong trends with Eddington ratio (Duras et al. 2020). Another study which integrates the $1 \mu\text{m} - 8 \text{keV}$ SED is consistent with Richards et al. (2006), suggesting $k_{\text{BC}} = 4.75$ for $\log(L_{3000}/\text{erg s}^{-1}) = 47.0$ (Runnoe et al. 2012). Significant differences in black hole mass or continuum luminosity between samples can have a second-order effect on the bolometric luminosity and hence the derived Eddington ratio by nature of the luminosity or Eddington ratio dependent bolometric correction.

In Figure 2, we present the Eddington ratio distribution of the sample collated in this study. The binned Eddington ratio abundances are volume-weighted using the $1/V_{\max}$ method and tabulated in Table 2. All of the quasars in the sample are accreting with $\lambda > 0.19$. We model the underlying Eddington ratio distribution with a log-normal function,

$$\rho_{\lambda} = \frac{1}{\sqrt{2\pi}\sigma_{\lambda}} \exp\left(-\frac{\log \lambda - \langle \log \lambda \rangle}{2\sigma_{\lambda}^2}\right), \quad (5)$$

where $\langle \log \lambda \rangle$ is the mean Eddington ratio, and σ_{λ} is the log standard deviation. Our Eddington ratio distribution, which peaks at $\langle \log \lambda \rangle = -0.21 \pm 0.03$ with $\sigma_{\lambda} = 0.30 \pm 0.02$ dex dispersion, is plotted with those of H24 at $z \sim 4$ and E-XQR-30+ (Mazzucchelli et al. 2023; D’Odorico et al. 2023; Fan et al. 2023) at $z \sim 6$, where each distribution is represented with a mean log-normal model and uncertainty reflected by the shaded region. We note that the three datasets are derived from surveys reaching different depths. Therefore, their Eddington ratio distribution functions are not directly comparable.

Furthermore, the E-XQR-30+ Eddington ratio distribution is not adjusted for incompleteness, because the dataset was compiled from inhomogeneous samples such that its selection function is not well-defined. The effect of a flux-dependent selection limit, if applied, is likely to broaden the $z \sim 6$ distribution and lower the mean Eddington ratio.

Although the Schechter function is frequently used to model the intrinsic Eddington ratio distribution, a log-normal function is well-matched to the low Eddington turnover, (e.g. Kollmeier et al. 2006; Willott et al. 2010b; Shen & Kelly 2012; Shen et al. 2019; Farina et al. 2022). We note that flux-limited detection limits can emulate the turnover and cause an underestimation of the low-Eddington population in the intrinsic distribution (e.g. Kollmeier et al. 2006; Schulze et al. 2015; Li et al. 2023). In the absence of low-Eddington constraints, we use the log-normal function to estimate the observed Eddington ratio distribution in our sample. However, as the selection function of the survey is based on the quasar luminosity, which is a product of the black hole mass and Eddington ratio, the Eddington ratio distribution can play a critical role in the mass function completeness (e.g. Kelly et al. 2009; Schulze & Wisotzki 2010). Any survey with a fixed flux limit would only include low-mass black holes with the highest Eddington ratios, and exclude high-mass black holes with exceptionally low Eddington ratios. The latter outcome, where supermassive black holes drop out of the parent survey’s flux limit due to low accretion rates and/or radiative efficiencies, can affect this study of the differential mass evolution if the intrinsic Eddington ratio distribution evolves over time.

A key question is whether a significant population of quiescent supermassive black holes exists at $z > 5$. High-redshift cosmological hydrodynamical simulations (e.g. Li et al. 2007; Sijacki et al. 2009; Bhowmick et al. 2022) find that accretion-driven growth becomes highly efficient by $z \sim 6$ and the most massive black holes are accreting close to the Eddington limit. This is in contrast to lower-redshift ($z < 4$) observations (e.g. Barger et al. 2005; Vestergaard & Osmer 2009; Kelly et al. 2010; Willott et al. 2010b) and simulations (e.g. Di Matteo et al. 2008; Sijacki et al. 2015; Volonteri et al. 2016), which find clear signatures of “cosmic downsizing” where the brightest AGN shift to lower black hole masses and the overall energy density production of AGN drops rapidly with decreasing redshift. One possibility to explain this occurrence is the preferential mass starvation of the most massive black holes at low redshift. These studies suggest that the most supermassive black holes at our redshift of interest ($z \sim 5$) are likely accreting quickly with high Eddington ratios, implying that the highest mass ($\log M_{\text{BH}}/M_{\odot} > 9.5$) bins in the $z \sim 5$ active black hole mass function could be highly complete in a luminosity-complete survey.

Recent data from the James Webb Space Telescope (JWST) has uncovered a surprisingly abundant population of faint AGN at $z > 4$ (e.g. Harikane et al. 2023; Maiolino et al. 2023; Yang et al. 2023; Matthee et al. 2024; Silk et al. 2024), lying above the local $M_{\text{BH}} - M_{*}$ relation (e.g. Pacucci & Loeb 2024; Li et al. 2024). Most of the black holes with mass estimates are reported to be between $M_{\text{BH}} \sim 10^6 - 10^8$ (e.g. Akins et al. 2023; Goulding et al. 2023; Harikane et al. 2023; Larson et al. 2023; Schneider et al. 2023; Übler et al. 2023). The most massive of these high redshift AGN have important consequences for studies of black hole seeding. Compared to extrapolations of the double power-law quasar luminosity function (Niida et al. 2020), the recent results have increased the abundance of faint AGN by over an order of magnitude (e.g. Harikane et al. 2023; Maiolino et al. 2023; Matthee et al. 2024). Our study, which focuses on the highest luminosity and most massive quasar subset, is not affected by the recent JWST revelations on the faint AGN population.

Table 2. Binned Eddington ratio distribution function for XQz5+ at $z \sim 5$ estimated by the $1/V_{\max}$ approach.

$\log L_{\text{bol}}/L_{\text{Edd}}$	N_{QSO}	$\Phi(L_{\text{bol}}/L_{\text{Edd}})$ $10^{-9} \text{ Mpc}^{-3} \text{ dex}^{-1}$
-0.63	5	0.70 ± 0.34
-0.45	12	1.98 ± 0.84
-0.26	24	2.44 ± 0.58
-0.08	17	1.74 ± 0.48
0.10	8	1.48 ± 0.78
0.29	5	0.57 ± 0.29
0.47	1	0.25 ± 0.25

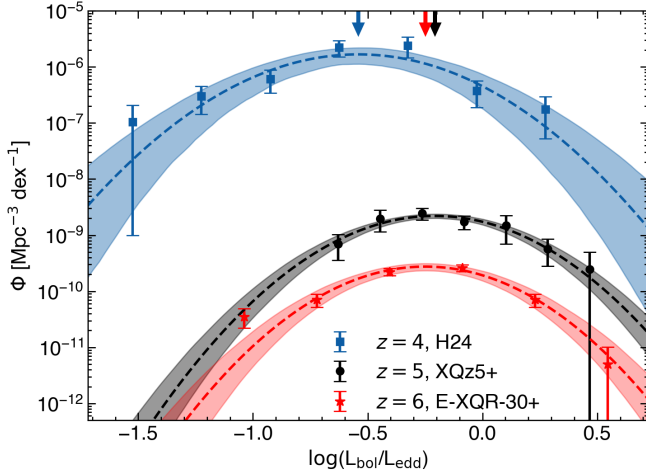


Figure 2. Eddington ratio distribution functions of XQz5+ (black circles) alongside H24 (blue squares) at $z \sim 4$ and E-XQR-30+ (red stars) at $z \sim 6$. Mass function model lines share the same colour as the points. The three datasets are derived from surveys which reach different depths. As such, their Eddington ratio distribution functions are not directly comparable. Furthermore, the E-XQR-30+ distribution function is not corrected for completeness. The Eddington ratio distribution of XQz5+ is best fit with a log-normal function, with a mean of $\langle \log \lambda \rangle = -0.21$ and the width of 0.30 dex. The mean value, indicated with the arrows on the top of the plot, is constrained to $\log(L_{\text{bol}}/L_{\text{Edd}}) = -0.54 \pm 0.06$ for H24, -0.21 ± 0.03 for XQz5+, and -0.25 ± 0.04 for E-XQR-30+.

2.3 Continuity equation

The time evolution of an accretion-dominated black hole mass function can be described by the following continuity equation (Shankar et al. 2013; Tucci & Volonteri 2017),

$$\frac{\delta \Phi(M_{\text{BH}}, t)}{\delta t} = - \frac{\delta [\langle \dot{M}_{\text{BH}} \rangle \Phi(M_{\text{BH}}, t)]}{\delta M_{\text{BH}}}, \quad (6)$$

where every black hole grows constantly at the mean accretion rate, $\langle \dot{M}_{\text{BH}} \rangle$. In practice, this picture is complicated by the duty cycle, which is the fraction of black holes in the active state, and merger events, which redistribute mass. To develop a more complete picture, we relate the Eddington ratio to the mass accretion rate by the radiative efficiency, $\epsilon \in (0, 1)$,

$$\dot{M}_{\text{BH}} = \frac{(1 - \epsilon)\lambda}{\epsilon} \frac{L_{\text{Edd}}}{c^2}, \quad (7)$$

which simplifies to an exponential mass growth with an e-folding time of $450\lambda^{-1}\epsilon(1 - \epsilon)^{-1}$ Myr (Salpeter 1964). In a more general picture,

the mean mass accretion rate can be written with the expectation value for Eddington ratio, which is

$$\langle \dot{M}_{\text{BH}} \rangle = \int d \log \lambda P(\lambda|M_{\text{BH}}, z) \lambda U(M_{\text{BH}}, z) \frac{M_{\text{BH}}}{450 \text{ Myr}} \frac{(1 - \epsilon)}{\epsilon}, \quad (8)$$

where $P(\lambda|M_{\text{BH}}, z)$ is the normalised Eddington ratio probability distribution and $U(M_{\text{BH}}, z) \in [0, 1]$ is the duty cycle. In this study, our approach is to observationally estimate the effective e-folding time under the assumption of time invariance of the radiative efficiency and Eddington ratio distribution as well as a constant duty cycle U over the observed period. We define a dimensionless growth rate scale factor,

$$k_{\text{ef}} \equiv \frac{450 \text{ Myr}}{t_{\text{ef}}} = \frac{\langle \lambda \rangle U (1 - \epsilon)}{\epsilon}, \quad (9)$$

which behaves as a joint constraint on the unknown parameters (ϵ , U), for an underlying Eddington ratio distribution, $P(\lambda|M_{\text{BH}}, z)$.

Standard thin accretion disc models predict that the radiative efficiency is a non-linear, but monotonic function of black hole spin. In the local universe, the fiducial value for the radiative efficiency based on the Soltan argument (Soltan 1982) applied to the local black hole mass density is $\epsilon = 0.1$ (Yu & Tremaine 2002), which corresponds to a black hole spin of $a \sim 0.7$. For individual quasars, observational constraints on the radiative efficiency can be obtained with X-ray reflection measurements or thermal continuum modelling (see review by Reynolds 2019). Estimates obtained from inhomogeneous quasar samples at higher redshifts are not significantly different from the local fiducial value (e.g. Capellupo et al. 2015; Vasudevan et al. 2016; Trakhtenbrot et al. 2017; Reynolds 2021, and references therein), which may be expected as massive black holes are spun up by prolonged periods of coherent accretion (Dotti et al. 2013; Volonteri et al. 2013; Dubois et al. 2014; Trakhtenbrot 2014; Capellupo et al. 2015; Ananna et al. 2020). However, radiatively inefficient accretion from uncorrelated flows (King et al. 2005, 2008) may be a mechanism by which the most extreme mass black holes could be produced at high redshift (King & Pringle 2006; Zubovas & King 2021).

Observational constraints on quasar lifetimes and duty cycle based on clustering suggest that luminous high-redshift (up to $z \sim 4 - 5$) quasars are biased towards rare massive haloes (Shen et al. 2007; White et al. 2008). Subsequent modeling efforts predict that the duty cycle must therefore be high, with $U \sim 0.5$ at $z \sim 4.5$ to $U \sim 0.9$ at $z \sim 6$ (Shankar et al. 2010), which is also supported by clustering simulations (DeGraf & Sijacki 2017). A high duty cycle implies that most of the massive black hole population in the mass function is reflected in observations. However, these results are at odds with measurements from the sizes of quasar proximity zones (e.g. Fan et al. 2006; Eilers et al. 2017, 2018; Khrykin et al. 2019; Eilers et al. 2020; Morey et al. 2021; Khrykin et al. 2021; Satyavolu et al. 2023b), which often measure lifetimes shorter than 10^7 yrs and sometimes $< 10^5$ yrs even at $z \sim 6$. One possible explanation for the discrepancy is that quasar light curves are described by a flickering model (Ciotti & Ostriker 2001; Novak et al. 2011; Oppenheimer & Schaye 2013; Schawinski et al. 2015; Davies et al. 2020; Satyavolu et al. 2023a) instead of a simple light bulb model. Proximity zone studies probe timescales of the most recent emission episode, which can be orders of magnitude shorter than the overall active fraction in a flickering model. Another possibility is that quasars spend a considerable amount of time growing in an obscured phase in their evolution (e.g. Hopkins et al. 2005), which implies a significant fraction of obscured quasars at high redshift (Davies et al. 2019; Ni et al. 2020; Satyavolu et al. 2023a), at a much higher ratio than

Table 3. Binned black hole mass function for XQz5+ at $z \sim 5$ estimated by the $1/V_{\max}$ approach.

$\log M_{\text{BH}}/M_{\odot}$	N_{QSO}	$\Phi(M_{\text{BH}})$ $10^{-9} \text{ Mpc}^{-3} \text{ dex}^{-1}$
8.68	4	0.65 ± 0.38
9.06	9	0.71 ± 0.25
9.45	18	1.40 ± 0.45
9.83	33	1.37 ± 0.26
10.21	7	0.21 ± 0.08
10.60	1	0.03 ± 0.03

observations at lower redshifts (e.g. Lawrence & Elvis 2010; Assef et al. 2015). Thus, the black hole mass function derived in this study would only reflect the active and unobscured subset of the underlying black hole population.

While black hole mergers do not alter the total mass in the population, they can still modify the shape of the mass function through redistribution. This can potentially affect the inferred evolution from the continuity equation if mergers play a critical role in growing the highest mass quasars over the probed redshift range. Theoretical and simulation-based works generally suggest that black hole mergers may play an important role at early times ($z \gtrsim 9$) to provide an early boost to black hole masses (Valiante et al. 2016; Bhowmick et al. 2022) and at late times ($z \lesssim 2$) when galaxies are comparatively gas-starved (Shankar et al. 2013; Dubois et al. 2014; Kulier et al. 2015). However, the majority of the assembled black hole mass can be attributed to secular processes (Martin et al. 2018). We also note that there are numerous studies in this space with a diversity of assembly histories capable of producing the high black hole masses observed at $z \sim 6$ (Li et al. 2007; Sijacki et al. 2009; Costa et al. 2014; Feng et al. 2014; Smidt et al. 2018; Valentini et al. 2021; Zhu et al. 2022), where the differences originate from the adopted accretion and feedback models. This highlights how continued work in this area will require improved observational constraints on high redshift supermassive black holes.

3 RESULTS AND DISCUSSION

We apply the model described in Section 2 to the XQz5+ data using the maximum likelihood approach and compare the result to the H24 $z \sim 4$ mass function. The observed evolution between these samples suggests an effective e-folding time for accretion-dominated growth based on the continuity equation. We compare this value to what we measure internally within our sample through the integrated mass density and we construct a mock universe simulation from the derived model mass functions to estimate Monte Carlo uncertainties. Finally, we discuss the implications of the measured mass evolution on the duty cycle and the radiative efficiency. We also derive the expected mass function at $z \sim 6$ and compare with results from the literature.

3.1 XQz5+ mass function and evolution

In this section, we first discuss the XQz5+ $z \sim 5$ binned black hole mass function. We then discuss two methods by which the dimensionless growth rate, k_{ef} in Equation 9, is estimated, either from redshifts $z = 5 - 4$ or within $z \sim 5$. We compare the results and use a mock universe simulation to estimate the Monte Carlo uncertainties.

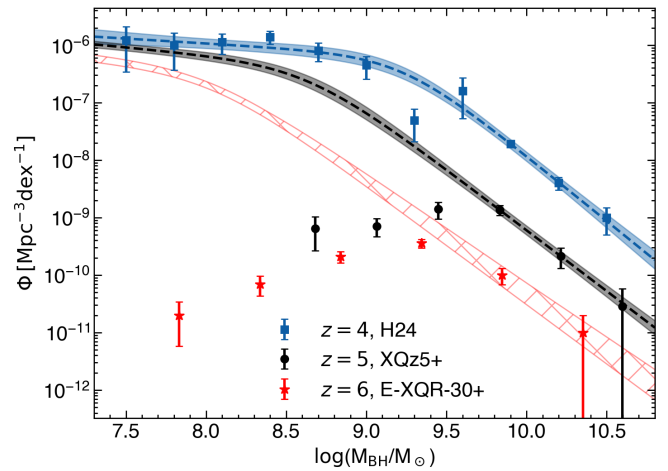


Figure 3. Black hole mass functions of XQz5+ (black circles) with H24 (blue squares) at $z \sim 4$ and E-XQR-30+ (red stars) at $z \sim 6$. The binned values are estimated with the $1/V_{\max}$ method, but the E-XQR-30+ mass function is not corrected for completeness. We plot the double power-law mass function models and the hatched model is the prediction for $z \sim 6$ assuming a constant growth of $k_{\text{ef}} = 1.79$, estimated from $z = 5 - 4$, and extrapolated onto $z \sim 6$ from $z \sim 5$.

In Figure 3, we present the binned mass function of XQz5+, measured with the $1/V_{\max}$ method as described in Equation 3. The black hole mass range of XQz5+ is subdivided into six equally-spaced bins in log-scale, where each bin is occupied by between $N_{\text{QSO}} = 1 - 33$ quasars. We present the tabulated abundances in Table 3 and each point is represented by the central black hole mass of the bin. The resulting XQz5+ black hole mass function exhibits an artificial turnover at $\log(M_{\text{BH}}/M_{\odot}) \lesssim 9.5$ due to the sample incompleteness. The mass function is resistant to changes in the number of bins. Therefore, we choose six bins to adequately resolve the position of the turnover while simultaneously maximising the number of quasars in each bin. The results of subsequent analyses are insensitive to the binning strategy.

In order to constrain the low-mass end of the XQz5+ mass function, we refer to H24, which has constrained the mass function at $z \sim 4$ in equally spaced bins down to $\log(M_{\text{BH}}/M_{\odot}) \sim 7.5$. We first fit their binned black hole mass function for their combined sample using the double power-law in Equation 4 and present the optimised parameters in Table 4 with associated uncertainties. The $z \sim 4$ mass function from H24 is then transformed to $z \sim 5$ with the continuity equation, optimising the mass accretion rate such that the transformed model fits the observed XQz5+ mass function at $\log(M_{\text{BH}}/M_{\odot}) \gtrsim 9.5$. After this, the double power-law is fit to the three most massive XQz5+ bins with the low-mass end constrained by the transformed $z \sim 4$ data. The optimised XQz5+ mass function parameters are presented in Table 4 with associated uncertainties.

3.1.1 Growth between $z = 5 - 4$

Both the H24 $z \sim 4$ and XQz5+ $z \sim 5$ binned mass function with their respective models are presented in Figure 3. The difference in the slopes of these mass functions is not statistically significant. However, the turnover mass, M_{BH}^* , has translated horizontally and the normalisation of the mass function also increases with cosmic time. This observable evolution from the $z \sim 5$ to $z \sim 4$ mass functions implies an effective growth scale factor of $k_{\text{ef}} = 1.79 \pm 0.01$, which is

fit to the highest mass data with the lowest uncertainties in H24. The k_{ef} error term does not include uncertainties in the mass functions, their completeness corrections, or cosmic variance, which are the dominant sources of uncertainty. To account for this, we model the systematic error from mock universe simulations in Section 3.1.3.

3.1.2 Growth within $z \sim 5$

As a sanity check, we independently measure the mass evolution within the XQz5+ sample. We bin the redshift range from $z = 4.5-5.2$ into N_{bin} shells of equivalent comoving volume. The redshift range, covering ~ 200 Myr, is selected where the completeness is more reliable and less affected by the details of interpolation. In each bin, we measure the completeness-corrected total mass of the N_{BH} most massive black holes. The critical assumption in this method is that the selected black holes in each redshift bin reflect a random sampling from an underlying population of the most extreme supermassive black holes that is growing with a mean population rate that then evolves into subsequent redshift bins. In principle, if the assumption holds true, the result would be more reliable for increasing quantities of N_{bin} shells and N_{BH} quasars. However, due to the limited size of the quasar sample, we fit the standard exponential accretion growth for all combinations of $N_{\text{bin}} = [4, 6]$ and $N_{\text{BH}} = [4, 10]$. The lower limit of $N_{\text{bin}} = 4$ and $N_{\text{BH}} = 4$ is least sensitive to completeness corrections, while the upper limit of $N_{\text{bin}} = 6$ and $N_{\text{BH}} = 10$ utilises almost all of the quasars in the XQz5+ sample. With this independent method, we find that quasars across the XQz5+ sample are evolving with $k_{\text{ef}} = 1.89 \pm 0.31$, representing the mean and standard deviation of all fits. The result is consistent with the observed growth in the ~ 360 Myr from redshifts $z = 5-4$ in Section 3.1.1.

3.1.3 Mock universe model

To test the robustness of the k_{ef} measurements, we simulate mock universes and estimate the Monte Carlo uncertainty. We anchor the simulator's reference mass function to the $z \sim 5$ model. The simulator functions by stepping through thin shells of comoving volume over a defined redshift range. We use the continuity equation to evolve the model mass function to the mean shell redshift for a prescribed k_{ef} , and an integrated number of quasars above a chosen mass threshold are randomly generated within each shell based on the probability distribution. The simulator reliably reproduces the reference $z \sim 5$ mass function with the expected Poissonian noise and predicts its evolution across redshifts.

We use the mock universe simulator to estimate the Monte Carlo uncertainty from measuring the mass evolution within the XQz5+ sample which covers ~ 200 Myr of time, finding a systematic uncertainty of $\sigma_{k_{\text{ef}}} = 0.5 - 0.8$ due to Poisson variance from small number statistics. The value of $\sigma_{k_{\text{ef}}}$ is sensitive to the width of the redshift range under consideration, where performing a measurement across a ~ 700 Myr width results in $\sigma_{k_{\text{ef}}} \sim 0.2$. The uncertainty is also dependent on the number of quasars counted in each bin, but does not change significantly with the number of bins, implying $\sigma_{k_{\text{ef}}} \propto (\sqrt{N_{\text{BH}} \Delta T})^{-1}$.

Furthermore, we determine the expected Monte Carlo uncertainty from measuring the k_{ef} derived from $z \sim 5$ to $z \sim 4$, finding a median absolute deviation of $\sigma_{k_{\text{ef}}} \sim 0.06$. Deriving the mass evolution factor between the XQz5+ and H24 dataset, each covering ~ 240 and ~ 360 Myr respectively with ~ 90 Myr separation, is less sensitive to cosmic variance than using the XQz5+ sample on its own.

The experiments performed with the mock universe simulator pro-

duce estimates of the uncertainty in the black hole mass growth measured from $z = 5-4$ and within $z \sim 5$ due to cosmic variance. Whichever the method, the uncertainty derived from the mock universe experiments is dominant over the measurement error and we find that this additional systematic uncertainty is most sensitive to the redshift coverage of the sample. We use the results of these experiments to define the statistical significance of our k_{ef} measurements.

3.2 Effective cosmic mass growth

The dimensionless growth factor, defined in Equation 9, is measured to be $k_{\text{ef}} = 1.79 \pm 0.01$ from the evolution between the $z \sim 5$ (XQz5+) and $z \sim 4$ (H24) mass functions or $k_{\text{ef}} = 1.89 \pm 0.31$ from the mass evolution within the XQz5+ sample using the integrated mass of the N_{BH} most massive in a range of redshift bins. The expected Monte Carlo uncertainty derived from the mock universe experiment is $\sigma_{k_{\text{ef}}} > 0.5$ for the mass evolution within XQz5+ and $\sigma_{k_{\text{ef}}} \sim 0.06$ for the change in the mass function from the $z \sim 5$ to $z \sim 4$ quasar samples. There is no evidence of a change in black hole mass growth rate within the $z \sim 5$ sample and from $z = 5-4$, due to the high uncertainty in the k_{ef} mass evolution within XQz5+. Therefore, our best estimate for the mass growth of supermassive black holes about $z \sim 5$ is $k_{\text{ef}} = 1.79 \pm 0.06$.

Based on these results, we present a surface plot in Figure 4, adopting a $k_{\text{ef}} = 1.79$ prescription. The plot shows joint constraints on the duty cycle and radiative efficiency for an estimated mean Eddington ratio in the underlying population. Contours of constant radiative efficiency are labelled and plotted as dashed lines. We overplot the expected value, $\langle \lambda \rangle$, of the log-normal Eddington ratio model for XQz5+, marking the mean and standard error with dotted lines. The expectation value is well-constrained to $\langle \log \lambda \rangle = -0.21 \pm 0.03$, or $\langle \lambda \rangle = 0.62 \pm 0.04$.

Assuming a fixed $k_{\text{ef}} = 1.79$ evolution in Figure 4, the growth between the $z = 5-4$ mass functions suggests that the underlying population of black holes could have mean radiative efficiencies of $\epsilon < 0.32$ (3σ of the $\langle \lambda \rangle$ scatter), depending on the duty cycle. However, because ϵ is a slow function of the dimensionless black hole spin, a_* , only the highest spin black holes are expected as radiatively efficient as $\epsilon > 0.30$. The results are also consistent with the fiducial $\epsilon = 0.10$ efficiency for a duty cycle of $U \sim 0.33$. Alternatively, if the average spin is biased towards low values ($0 \leq |a_*| \leq 0.3$) expected for chaotic accretion (e.g. King et al. 2008; Berti & Volonteri 2008), then the duty cycle would be in the range $U = 0.18 - 0.22$.

If the high-redshift massive black hole population duty cycle is as low as $U \sim 0.1$, suggested by the simple light bulb model in proximity zone studies (e.g. Khrykin et al. 2021), then the observed growth would require the accretion radiation feedback to be inefficient ($\epsilon \sim 0.03$), which implies that the accretion disc and the black hole spin are counter-aligned. This scenario is plausible if the massive black hole population primarily grows through short episodes of uncorrelated flows (King & Pringle 2006), which prevents the black hole from spinning up (e.g. King et al. 2005; Lodato & Pringle 2006). Spin misalignment, expected from infalling material that is insensitive to the spin direction of the inner accretion disc, could also result in severely warped structures in the accretion disc (e.g. Chatterjee et al. 2020), which can obscure the broad-line region (Lawrence & Elvis 2010). This is also consistent with the prediction of a significant population of obscured quasars at high redshift (e.g. Davies et al. 2019), which we discuss further in Section 3.3.1. Low radiative efficiencies can also be the result of photon trapping in supercritically accreting thick discs (e.g. Ohsuga et al. 2002; Wyithe & Loeb 2012).

Conversely at high duty cycles, the measured growth is consistent

Table 4. Optimised fit parameters for the black hole mass function double power-law in Equation 4. We fit the model to datasets spanning different redshift ranges. The bolded parameters represent the $z \sim 5$ mass function maximum likelihood fit from this study.

Redshift	Dataset	$\Phi(M_{\text{BH}}^*)$ $10^{-7} \text{ Mpc}^{-3} \text{ dex}^{-1}$	M_{BH}^* $10^x M_{\odot}$	α	β
$3.50 < z < 4.25$	He et al. (2024)	6.6 ± 2.1	9.23 ± 0.09	-1.17 ± 0.12	-3.26 ± 0.15
$4.50 < z < 5.30$	This work	4.6 ± 1.3	8.64 ± 0.11	-1.26 ± 0.09	-3.12 ± 0.11
$5.80 < z < 6.40^*$	D’Odorico et al. (2023); Fan et al. (2023)	3.7 ± 1.3	8.10 ± 0.11	-1.31 ± 0.11	-3.04 ± 0.09

*Fit to mock universe model, with uncertainties adopted from the $z \sim 5$ model.

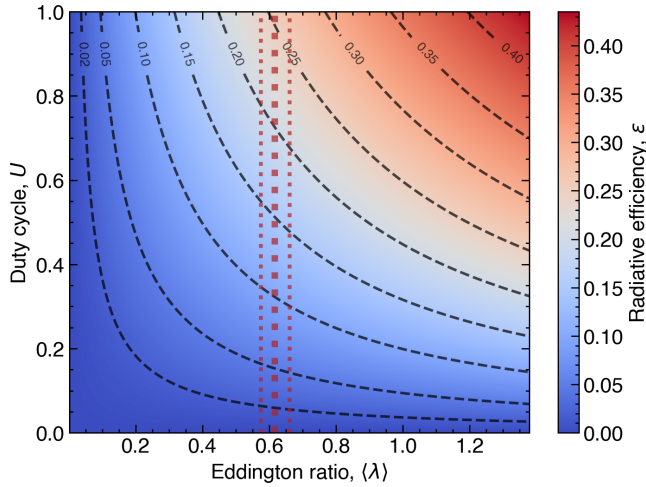


Figure 4. Surface plot showing the relationship between the Eddington ratio, duty cycle, and radiative efficiency satisfying Equation 9 for $k_{\text{ef}} = 1.79$. We overplot dashed radiative efficiency contours and the uncertainty on the expected value of the XQz5+ Eddington ratio log-normal model as the solid line, which is described by a mean and width of $\langle \log \lambda \rangle = -0.21 \pm 0.03$ dex, shown as vertical dotted lines.

with a population of quasars that have been spun up by coherent accretion flows over long episodes. Such high duty cycles are consistent with clustering studies (e.g. Shen et al. 2007; White et al. 2008), but the constraints on the inferred lifetimes are weak owing to uncertainties in models of quasar-hosting dark matter haloes (e.g. Shen et al. 2009; Cen & Safarzadeh 2015). Additional clarity on the high-redshift quasar duty cycle will enable firmer conclusions on the implied black hole spin, based on the observed mass evolution.

3.3 Comparison to $z \sim 6$

In Figure 3, we show the $z \sim 6$ mass function measured from the E-XQR-30+ database using the $1/V_{\text{max}}$ approach without applying completeness corrections. The predicted $z \sim 6$ model from our study, represented with the hatched region, is extrapolated from the dimensionless growth factor of $k_{\text{ef}} = 1.79 \pm 0.06$ derived between $z = 5 - 4$. The optimised $z \sim 6$ double power-law fit parameters are presented in Table 4 with parameter uncertainties adopted from the $z \sim 5$ model.

We remark that despite the absence of a completeness correction, the two highest mass binned points of E-XQR-30+ are consistent with the model expectation. Taken at face value, this result would imply that E-XQR-30+ is highly complete ($\Omega(L, z)f_{\text{obs}} > 0.5$) at the high mass end and it disfavours scenarios where the black holes evolve more rapidly between $z = 6 - 5$ than $z = 5 - 4$. This observation is at odds with the general expectation that black holes in the early

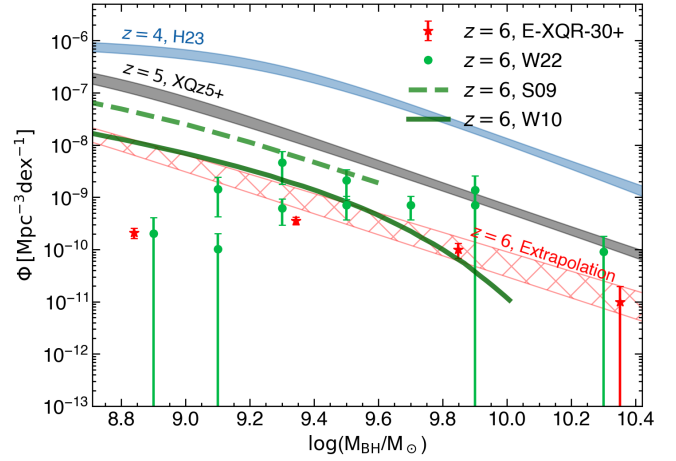


Figure 5. Literature estimates of the $z \sim 6$ active black hole mass function compared to the mass function models from Table 4 at redshifts $z = 6 - 4$, with the same identifying characteristics as in Figure 3. The active black hole mass functions of Willott et al. (2010b) (green solid line), Shankar et al. (2009) (green dashed line), Wu et al. (2022) (green points), and E-XQR-30+ (red stars) are shown. In some of the Wu et al. (2022) mass bins, there are two spatial density estimates, because they consider two quasar samples, each with their own completeness function. We have not corrected E-XQR-30+ for completeness due to heterogeneity in its sample construction.

Universe need to evolve quickly to reach their observed masses and are decelerating in their growth as seen in the cosmic downsizing phenomenon (e.g. Barger et al. 2005).

We compare the predicted $z \sim 6$ black hole mass function model with several other empirical studies of quasar demographics at $z \sim 6$ (Shankar et al. 2009; Willott et al. 2010b; Wu et al. 2022). Compared to semi-analytical or simulation-based models (e.g. Li et al. 2007; Kulier et al. 2015; Amarantidis et al. 2019; Piana et al. 2021), the methods used to derive these empirical mass functions are more directly comparable to the approach adopted in this study. In Figure 5, we overplot the three literature $z \sim 6$ active black hole mass functions with H24 ($z \sim 4$), XQz5+ ($z \sim 5$), and the extrapolated $z \sim 6$ black hole mass functions presented in Table 4. We also plot the uncorrected binned mass function derived from the E-XQR-30+ database, showing that the literature mass functions generally predict higher quasar abundances. E-XQR-30+ is a much larger heterogeneously constructed sample of quasars with Mg II-based black hole mass estimates and it serves as a sensible lower-bound for the $z \sim 6$ quasar space density. The mass functions from Shankar et al. (2009) and Willott et al. (2010b) have been corrected to the active black hole mass function by removing their duty cycle and obscuration fraction corrections. At the high mass end, we observe that the Wu et al. (2022) $z \sim 6$ spatial densities are of similar magnitude as our XQz5+

$z \sim 5$ sample while the Shankar et al. (2009) mass function lies above our $z \sim 6$ extrapolated model for all masses. In the following discussion, we explore each of the $z \sim 6$ literature mass functions in detail.

The mass function from the Shankar et al. (2009) study was the result of models fit to the local black hole mass function, the X-ray background, and the luminosity functions at a variety of redshifts up to $z \sim 6$. The black hole masses are translated to luminosities by assuming a constant Eddington ratio of $\lambda = 0.4$ and radiative efficiency of $\epsilon = 0.065$, while the duty cycle $U(z = 6, \log M_{\text{BH}} = 9.5) = 0.5$ is a function of mass and redshift. They have also adopted a correction for the obscured fraction, which is sensitive to AGN luminosity (e.g. Lawrence 1991; Willott et al. 2000; Ueda et al. 2003; Hasinger 2008; Merloni et al. 2014; Ueda et al. 2014), and they used the luminosity-dependent observable fraction, parameterised with a power-law by Hopkins et al. (2007). We invert the obscuration correction to derive the Shankar et al. (2009) active black hole mass function. In the Shankar et al. (2009) reference model, the duty cycle is relatively flat for high mass ($\log(M_{\text{BH}}/M_{\odot}) > 9.0$) black holes, falling from $U(6, 9.5) = 0.5$ to $U(5, 9.5) = 0.2$ and subsequently $U(3, 9.5) = 0.07$. Under this model, much of the mass assembly would already have occurred at even higher redshifts in order for the results to match the local black hole mass function. Thus, in light of the strong duty cycle evolution and difference in radiative efficiency, it is not surprising that the spatial densities in the Shankar et al. (2009) mass function is higher at all masses than our extrapolated mass function.

The analysis from Willott et al. (2010b) assumes $\epsilon = 0.09$, a distribution of Eddington ratios centred at $\lambda = 0.6$ with a dispersion of 0.3 dex, and a uniform duty cycle distribution between $U = 0.5 - 1.0$. This model is fit to the Willott et al. (2010a) $z \sim 6$ luminosity function based on 40 quasars. Similar to Shankar et al. (2009) study, an additional correction factor for obscured quasars was applied, which we have inverted to estimate the active black hole mass function. The Willott et al. (2010b) black hole mass function was determined to be considerably lower than the Shankar et al. (2009) mass function by a factor of ~ 3 . We find that Willott et al. (2010b) is consistent with the extrapolated $z \sim 6$ mass function in this study at lower masses, but the high-mass slope is steeper and underestimates the abundance of massive quasars.

The Wu et al. (2022) mass function utilised a sample of 29 quasars with mostly Mg II-based virial black hole mass estimates and just over 100 quasars with M_{1450} estimates from a fixed power-law continuum extrapolation. The quasars with black hole mass estimates are split into two samples (see Jiang et al. 2016), hence there can be two estimates for the spatial density in the same mass bin. At high masses, the Wu et al. (2022) binned spatial density is more consistent with the $z \sim 5$ spatial density than with other $z \sim 6$ mass functions, but the two highest mass bins which appear to deviate from the mass function of Willott et al. (2010b), contain only 5 quasars, including J0100+2802 ($z = 6.3$), which is the sole occupant of the highest mass bin. The derived spatial densities are then boosted by large correction factors. The black hole mass of J0100+2802 adopted in Wu et al. (2022) is arguably mildly overestimated based on new James Webb Space Telescope spectra (Eilers et al. 2023). Furthermore, no other object in the E-XQR-30+ database, which includes quasars over a much larger sky area, has a measured luminosity comparable to J0100+2802, which is more luminous by a factor of ten over the second most luminous quasar. This makes J0100+2802 a one-of-a-kind outlier at its redshift.

Furthermore, while the redshift coverage of Wu et al. (2022) extends to $z = 6.42$, the space between $6.31 < z < 6.42$ is void of

any quasars and two of the three quasars at $z > 6.3$ are among the four most massive quasars in the Wu et al. (2022) sample such that excluding quasars at the under-complete $z > 6.3$ space has a dramatic effect on the mass function in the highest mass bins. By excluding quasars at $z > 6.3$, the Wu et al. (2022) binned mass function at $\log(M_{\text{BH}}/M_{\odot}) > 9.2$ becomes consistent within 1σ with the $z \sim 6$ extrapolated model.

A mass growth factor of $k_{\text{ef}} = 1.5 - 1.8$ can be measured between the Wu et al. (2022) $z \sim 6$ and the H24 $z \sim 4$ binned mass functions. Although the result is consistent with the $z = 5 - 4$ growth rate, the Wu et al. (2022) completeness corrections are highly uncertain (L. Jiang, priv. comm.).

In the following sections, we list and discuss several limitations in our study that can affect the measured growth rate, the extrapolation to $z \sim 6$, and explanations for discrepancies between mass functions from different studies.

3.3.1 Overestimated completeness?

It is possible that the high flux completeness, $\Omega(L, z)$, of our parent sample at $z \sim 5$ does not translate directly to a high completeness in black hole mass as previously assumed. This would be the case if there exists a significant fraction of obscured, quiescent, or low-Eddington quasars with massive black holes. If the active fraction also evolves over the redshift range of $z = 6 - 4$, then the differential correction across mass functions at different redshifts would also capture this time-dependence, limiting the ability to interpret the observed growth in terms of accretion properties. There are indications that the obscured fraction is more significant at higher redshifts than at lower redshifts (e.g. Davies et al. 2019; Vijarnwannaluk et al. 2022), which would cause the mass functions to diverge. Clustering studies suggest that changes to the obscuration fraction may be secondary to the redshift evolution in the duty cycle (Porciani et al. 2004; Porciani & Norberg 2006; Shen et al. 2007), which describes a general decline in quasar activity over the age of the universe across all masses. The high space density in the massive black hole population observed at $z \sim 4$ (He et al. 2024) and the consistency in the mass function slope in the $z = 6 - 4$ redshift range suggest that the most massive black holes have yet to turn off and move to lower luminosities, as described by cosmic downsizing (e.g. Barger et al. 2005; Vestergaard & Osmer 2009; Kelly et al. 2010). In order to reliably correct for these effects, more work is needed to understand the population of obscured quasars and the quasar duty cycle at high redshift.

3.3.2 Overestimated black hole masses?

Overestimated black hole masses can have a significant effect on the black hole mass function. Black hole masses can be overestimated in a systematic fashion when measurements of the most massive black holes are the result of the long tail of the virial black hole mass estimate error function or when mass estimates are derived from different emission-lines with separate calibrations. We first remark that the H24 $z \sim 4$ black hole masses are derived from the broad C IV emission-line, whereas the $z \sim (5, 6)$ samples use the Mg II line. The C IV line is more likely to be affected by non-virial motions (e.g. Proga et al. 2000; Richards et al. 2011; Shen & Liu 2012; Trakhtenbrot & Netzer 2012; Mejía-Restrepo et al. 2018; Saturni et al. 2018), which motivated the addition of correction factors to the mass calibration accounting for, among others, the C IV blueshift (Coatman et al. 2016, 2017, e.g.) and the peak flux ratio of the

C IV line with other UV emission lines (e.g. Runnoe et al. 2013; Mejía-Restrepo et al. 2016). H24 also investigated an alternative mass calibration (Park et al. 2017), which sought to compensate for the peculiarities of C IV. This led to a much tighter black hole mass distribution centred at lower masses, which would imply a steeper bright-end slope and lower-mass turnover in the $z \sim 4$ mass function. Our analysis would then have overestimated the growth in the most massive black holes between $z = 5 - 4$. However, H24 ultimately disfavoured this alternative scenario on account of the lack of high-mass calibration sources and the abandonment of a virial-like dependence on the line width.

Black hole masses estimated from single-epoch virial mass estimates depend on a high-luminosity extrapolation of the radius-luminosity relationship from reverberation mapping experiments (McLure & Dunlop 2004; Shen et al. 2011). Reverberation mapping campaigns focused on high-redshift and high-luminosity quasars are expensive due to the large broad-line region sizes and cosmological time dilation, which necessitates long-term monitoring programmes. Recent results on high-luminosity quasars (e.g. Lira et al. 2018; Hoormann et al. 2019; Grier et al. 2019; Kaspi et al. 2021) suggest a shallower radius-luminosity than measured in McLure & Dunlop (2004), which is more consistent with the photoionisation expectation of $R \propto L^{0.5}$. Black hole masses that are over-sensitive to the observed luminosity could obfuscate the underlying mass growth rates of the population, artificially boosting the apparent mass evolution when there is luminosity evolution.

Another way that the black hole masses can be overestimated is if they represent the tail end of the virial black hole mass error function. Because of the precipitous decline in abundance in the high mass regime, lower-mass black holes are more likely to be scattered high by a symmetric error function. The H24 derivation of the intrinsic black hole mass function accounting for the error function estimated a high-mass slope of $\beta \sim -6$ as opposed to the $\beta \sim -3$ measured in Table 4. However, our quasars are selected by luminosity and not black hole mass, which is proportional to mass by $M_{\text{BH}} \propto L^b$ in Equation 2, where $b = 0.5$ under standard photoionisation calculations and $b = 0.62$ in the Shen et al. (2011) calibration. This has a weaker effect on the black hole mass than the measured full-width at half maximum, to which the black hole mass is correlated by $M_{\text{BH}} \propto \text{FWHM}^2$, based on the virial theorem. Because the scatter in FWHM is not systematically biased by our luminosity selection, mass bias resulting from a fixed homoscedastic virial mass estimate error distribution would cancel out in a differential growth analysis between redshifts.

3.3.3 Slower growth between $z = 6 - 5$?

The $1/V_{\text{max}}$ binned mass function measured with the E-XQR-30+ database disfavours scenarios where the mass growth between $z = 6 - 5$ is more rapid than between $z = 5 - 4$. Instead, the completeness corrected $z \sim 6$ active black hole mass functions (Shankar et al. 2009; Willott et al. 2010b; Wu et al. 2022) suggest that the evolution from $z = 6 - 5$ could be even more gradual, which is counter to the general expectation that black holes in the early Universe need to evolve quickly to match observed masses at high-redshift. In principle, the slow growth of massive black holes from $z = 6 - 5$ can be caused by cosmic downsizing, where the highest mass black holes are experiencing preferential mass starvation and turning off, but it is inconsistent with the more rapid growth seen between $z = 5 - 4$, unless the black hole masses in H24 are overestimated by uncorrected C IV virial estimates.

The evolution of the quasar luminosity function is potentially en-

hanced between $z = 6.0 - 5.5$ compared to $z = 5.5 - 5.0$ (Kashikawa et al. 2015; Giallongo et al. 2019; Grazian et al. 2020; Santos et al. 2021). However, a constant evolution in the quasar luminosity function across the end of reionisation epoch between $z = 6 - 5$ is not excluded. Based on the comparison with literature $z \sim 6$ mass functions and the mass function extrapolated from the measured growth between $z = 5 - 4$, our analysis indicates that the mean rate of change in the black hole mass function between $z = 6 - 5$ is consistent with $z = 5 - 4$, implying no change in the mass growth rate across $z = 6 - 4$.

3.3.4 Additional remarks

New luminosity function analyses at high redshift focusing on bright quasars (Onken et al. 2022; Grazian et al. 2022) updated previous determinations (e.g. Yang et al. 2016; McGreer et al. 2018; Niida et al. 2020) with an increased space density of bright quasars. This result was prefaced by surveys of the ultraluminous quasar population (e.g. Schindler et al. 2017, 2019a; Boutsia et al. 2020; Cristiani et al. 2023) which showed that previous surveys had underestimated their completeness corrections by $\sim 30\%$ (Schindler et al. 2019b; Boutsia et al. 2021). In the black hole mass function context, Wu et al. (2022) attributed their high-mass divergence from Willott et al. (2010b) to their inclusion of an error model, which implies that the virial black hole masses of quasars within their highest mass bins are possibly overestimated. However, applying an upper redshift threshold of $z = 6.3$ to Wu et al. (2022), as discussed in Section 3.3.2, corrects their mass function to within 1σ of our model extrapolation from the observed $z = 5 - 4$ k_{ef} growth. We expect that discrepancies between mass functions derived from heterogeneous methods to be an unavoidable consequence of the multitude of correction factors, broad scatter from uncertainties in the black hole mass and luminosity determinations, as well as cosmic variance. This highlights the importance of wide-area surveys of high completeness, as well as the need for improving the accuracy of black hole mass measurement techniques.

3.4 Black hole initial mass function

Although there are a few supermassive ($> 10^{10} M_{\odot}$) black holes in XQz5+, this dataset does not produce the most stringent constraints on black hole seeds due to their relatively low redshift compared to billion solar mass black holes observed at $z > 7$ (e.g. Mortlock et al. 2011; Bañados et al. 2018; Wang et al. 2018; Yang et al. 2019, 2020). More recently, the James Webb Space Telescope enabled the search of AGN to push into higher redshifts (e.g. Larson et al. 2023), leading to the highest redshift AGN ($z \sim 10$) discovery thus far, revealed by its X-ray emission as seen by the Chandra X-ray Observatory (Bogdán et al. 2024). Its mass was inferred to be $10^7 - 10^8 M_{\odot}$, comparable to the stellar mass of its host, which would require heavy seeds of $10^4 - 10^5 M_{\odot}$ even with constant accretion at the Eddington limit.

Using the $z \sim 5$ black hole mass function model derived in this study, we trace the evolution of the mass function back to $z = 20$ (~ 175 Myr post Big Bang), which is an accessible redshift for the future Laser Interferometer Space Antenna (Amaro-Seoane et al. 2017). We derive the hypothetical initial mass function at $z = 20$ that would be consistent with the observed $z \sim 5$ mass function for effective growth $k_{\text{ef}} = 1 - 9$, where $k_{\text{ef}} = 9$ is the growth rate of a black hole that is growing without stopping at the Eddington limit with the fiducial radiative efficiency of $\epsilon = 0.1$. Figure 6 presents the $z = 20$ initial mass functions with proposed seeding mechanisms and their associated seed masses: Pop III remnants ($< 10^3 M_{\odot}$),

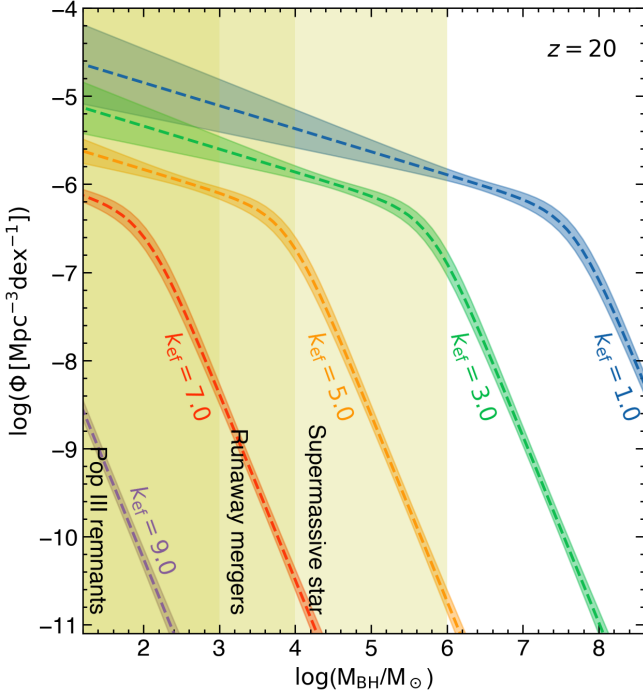


Figure 6. Black hole mass functions evolved to $z = 20$ through the continuity equation based on the reference mass function model at $z \sim 5$ and effective dimensionless growth parameters, $k_{\text{ef}} = 1 - 9$, where $k_{\text{ef}} = 9$ is the growth rate of a black hole growing 100% of the time with an Eddington ratio of $\langle \lambda \rangle = 1$ and radiative efficiency of $\epsilon = 0.1$. Overplotted are three proposed seeding mechanisms for the most massive high-redshift black holes and their seed mass range: Pop III remnants ($< 10^3 M_{\odot}$), runaway mergers ($10^3 - 10^4 M_{\odot}$), and supermassive star collapse ($10^4 - 10^6 M_{\odot}$) (see review from Inayoshi et al. 2020). A $z = 20$ reference redshift for the initial black hole mass function corresponds to ~ 175 Myr after the Big Bang.

runaway mergers ($10^3 - 10^4 M_{\odot}$), and supermassive star collapse ($10^4 - 10^6 M_{\odot}$) (Inayoshi et al. 2020). Black holes would need to grow at $k_{\text{ef}} > 5.0$ since their formation at $z = 20$ in order for the observed mass function to be consistent with the maximum mass of heavy seeds. Even the most massive black holes of XQz5+ are consistent with Pop III remnants if allowing for perpetual Eddington limited growth at the fiducial radiative efficiency of $\epsilon = 0.1$. Unlike supermassive black holes at redshifts $z > 6$, the lower redshift black holes are not as strongly limited by the available cosmic time and thus there are multiple channels of mass assembly that are consistent with the observed spatial and mass densities.

In Figure 7, we estimate the redshift at which a $10^4 M_{\odot}$ black hole would need to be born by to produce a black hole with $10^{10} M_{\odot}$ by $z = 5$, given a particular growth rate, k_{ef} . We choose $10^4 M_{\odot}$ as the fiducial seed mass because it is the interface between two of the heavy seed mechanisms: supermassive star collapse and runaway merger from a dense stellar cluster. We have set an upper limit to the birth redshift at $z = 30$, which corresponds to ~ 100 Myr age for the universe. The results show that $10^4 M_{\odot}$ seeds could not produce the observed ten billion solar mass black holes by $z = 5$ unless the mean growth rate exceeds $k_{\text{ef}} = 6.2$. As shown in Figure 8, the joint constraints on the radiative efficiency, Eddington ratio, and duty cycle from a growth rate of $k_{\text{ef}} > 6$ would exclude $\epsilon > 0.14$ for Eddington limited accretion.

In Figure 7, black holes with masses $\log(M_{\text{BH}}/M_{\odot}) \gtrsim 9.5$ at

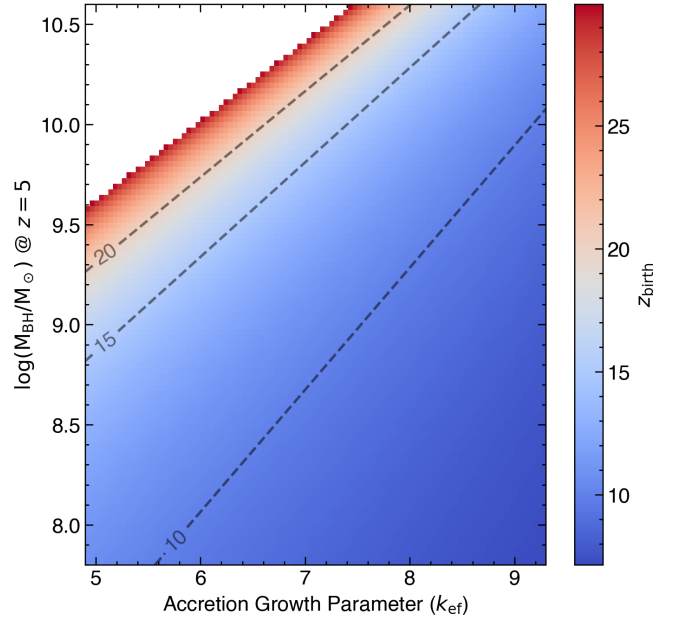


Figure 7. Redshift of $10^4 M_{\odot}$ black hole seed birth required to accrete a black hole of a specific mass by redshift $z = 5$ for a variety of accretion growth rates. The white exclusion region is set by an upper redshift limit of $z = 30$, which corresponds to an age of ~ 100 Myr. The ten billion solar mass black holes observed in XQz5+ are only consistent with $10^4 M_{\odot}$ black hole seeds if the accretion growth rate is ~ 3.5 times the observed growth between $z = 5 - 4$ mass functions.

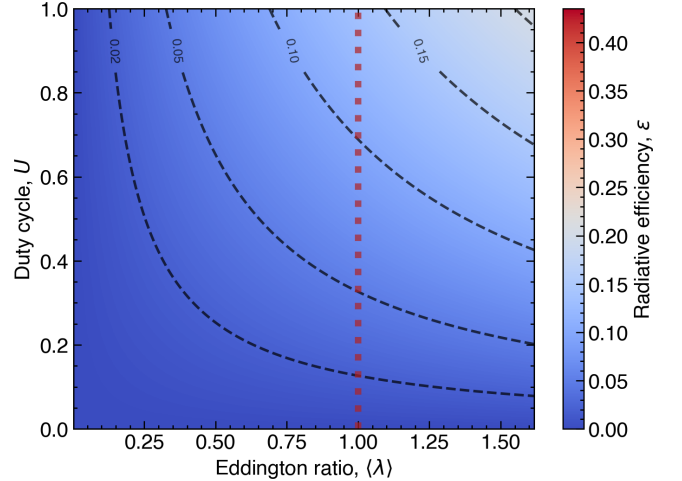


Figure 8. Surface plot showing the relationship between the Eddington ratio, duty cycle, and radiative efficiency satisfying Equation 9 for $k_{\text{ef}} = 6.2$. We overplot dashed radiative efficiency contours and highlight $\langle \lambda \rangle = 1.0$ with the vertical dashed line.

$z \sim 5$ are excluded by the upper redshift limit $z_{\text{max}} = 30$ when $k_{\text{ef}} = 5$ and the seed mass is $10^4 M_{\odot}$. The majority of XQz5+ black holes are more massive than $\log(M_{\text{BH}}/M_{\odot}) = 9.5$, which provides evidence that the rate of growth by accretion in the early universe is likely to be a factor of ~ 3.5 higher than observed between $z = 5 - 4$. If the seed mass is within the range of $10^{5-6} M_{\odot}$ instead, indicative of a direct collapse heavy black hole seed, then growth rates ~ 3 times that of $z = 5 - 4$ is sufficient to explain the $z \sim 5$ mass function

with $z_{\text{birth}} = 30$ as shown in Figure 6. Otherwise, if faster evolution is not occurring at higher redshifts, a growth factor of $k_{\text{ef}} = 1.79$ extrapolated to $z = 30$ would require seeds of $\sim 10^{8.2} M_{\odot}$ to produce $10^{10} M_{\odot}$ black holes by $z = 5$.

4 SUMMARY AND CONCLUSION

In this study, we analyse the black hole mass function at $z \sim 5$ and compare to mass functions at $z \sim 4$ and $z \sim 6$. We measure the evolution in the mass function between $z = 5 - 4$ using the continuity equation and present joint constraints on the duty cycle, radiative efficiency, and mean Eddington ratio. Finally, we discuss the implications of our study on the population of black hole seeds in the early universe. The main results of this study are summarised:

- Our sample, collated from [Lai et al. \(2024\)](#), [Trakhtenbrot et al. \(2011\)](#), and [López et al. \(2016\)](#), collectively referred to as XQz5+, is composed of 72 of the most luminous quasars with spectroscopic follow-up observations over the redshift range $4.5 < z < 5.3$. The black hole masses of the quasars in the sample are measured using the single-epoch virial mass estimate based on the Mg II broad emission-line in their respective studies. We use the $1/V_{\text{max}}$ approach (Eq. 3) to derive population distribution functions and present our completeness corrections in Figure 1. Our sample occupies a highly complete parameter space, enabling further demographic analysis.

- The Eddington ratio distribution function for XQz5+ (Fig. 2) is consistent with a log-normal function centered around $\langle \log \lambda \rangle = -0.21 \pm 0.03$, with dispersion $\sigma_{\lambda} = 0.30 \pm 0.02$ dex. In comparison to other observed Eddington ratio distributions at lower ([He et al. 2024](#)) and higher ([D’Odorico et al. 2023](#)) redshifts, the Eddington ratio distribution of XQz5+ is centered on a higher value, but the dispersion is comparable.

- The mass function of XQz5+ (Fig. 3) is consistent with a power-law on the high-mass regime with an artificial turnover at $\log (M_{\text{BH}}/M_{\odot}) \lesssim 9.5$ caused by incompleteness. We model the mass function with a double power-law (Eq. 4) using the low-mass constraints of [He et al. \(2024\)](#) translated from $z \sim 4$ to $z \sim 5$. The evolution from XQz5+ to the [He et al. \(2024\)](#) mass function implies an accretion growth factor of $k_{\text{ef}} \equiv \langle \lambda \rangle U(1 - \epsilon)/\epsilon = 1.79 \pm 0.06$, where λ is the Eddington ratio, U is the duty cycle, and ϵ is the radiative efficiency. Cosmic variance is the dominant source of error in the measured mass growth rate.

- We extrapolate the measured evolution of the black hole mass function from $z = 5 - 4$ to $z \sim 6$, comparing against the existing literature in Fig. 5 and a high-redshift comparison sample composed of XQR-30 ([D’Odorico et al. 2023](#)) augmented by the [Fan et al. \(2023\)](#) compilation, which we call E-XQR-30+. Although the binned black hole mass function of E-XQR-30+ is qualitatively similar to our $z \sim 6$ prediction, a detailed analysis is reserved for a future study due to heterogeneity in the sample construction and uncertainty in its completeness function.

- We also estimate $k_{\text{ef}} = 1.89 \pm 0.31$ within the XQz5+ sample with an additional $0.5 - 0.8$ in systematic uncertainty due to cosmic variance. This result is consistent with the growth measured between $z = 5 - 4$.

- If the mean mass growth rate observed at $z \sim 5$ is extended to an initial mass function at $z \sim 20$, the seed mass required to form a $10^9 M_{\odot}$ black hole by $z \sim 5$ would be $> 10^7 M_{\odot}$. Therefore, we find that the mean mass evolution in the early universe would need to be a factor of $\gtrsim 3 - 4$ times the rate measured between $z \sim 5 - 4$ to be consistent with heavy seed masses from exotic black hole formation mechanisms (Fig. 6).

From this study, we infer that the black hole mass growth has slowed considerably by $z \sim 5$ and would have had to been more rapid in the early Universe. For accretion-dominated mass growth, this imposes more stringent constraints on the Eddington ratio, radiative efficiency, and duty cycle unless supercritical growth is achieved and maintained over extended durations. Improvements to these measurements will require measuring black hole masses for a larger sample of quasars over a wider area of the sky or expanding the survey flux limit. Improved statistics would allow for more advanced statistical modelling techniques to produce reliable joint constraints on distributions of black hole properties. Additionally, an enhanced understanding of the obscured quasar fraction across the relevant redshift and luminosity ranges would further refine our result. Future constraints on quasar demographics at higher redshift will depend on the results from new facilities such as the James Webb Space Telescope, which will enable black hole mass measurements from the H β emission-line between redshifts $5 < z < 10$. The first homogeneous samples at such high redshifts will illuminate the circumstances that gave rise to the accelerated growth required for prospective supermassive black holes to reach their observed masses by $z \lesssim 7$. The future Laser Interferometer Space Antenna has the capability for direct detections of black hole mergers with total participating masses of $\sim 10^4 - 10^7$ beyond redshifts of $z \sim 20$, probing the activity of newly-born massive seeds before they lose the memory of their birth.

ACKNOWLEDGEMENTS

We are grateful to the anonymous referee whose contribution has improved this study.

S.L. is grateful to the Research School of Astronomy & Astrophysics at Australian National University for funding his Ph.D. studentship.

CAO was supported by the Australian Research Council (ARC) through Discovery Project DP190100252.

This paper is based on observations made with ESO Telescopes at the La Silla Paranal Observatory under programme IDs 084.A-0574(A), 084.A-0780(B), 087.A-0125(A), 094.A-0793(A), 098.A-0111(A), 0100.A-0243(A), 0104.A-0410(A), 108.22H9.001, 109.23D1.001, and 109.23D1.002.

The national facility capability for SkyMapper has been funded through ARC LIEF grant LE130100104 from the Australian Research Council, awarded to the University of Sydney, the Australian National University, Swinburne University of Technology, the University of Queensland, the University of Western Australia, the University of Melbourne, Curtin University of Technology, Monash University and the Australian Astronomical Observatory. SkyMapper is owned and operated by The Australian National University’s Research School of Astronomy and Astrophysics. The survey data were processed and provided by the SkyMapper Team at ANU. The SkyMapper node of the All-Sky Virtual Observatory (ASVO) is hosted at the National Computational Infrastructure (NCI). Development and support of the SkyMapper node of the ASVO has been funded in part by Astronomy Australia Limited (AAL) and the Australian Government through the Commonwealth’s Education Investment Fund (EIF) and National Collaborative Research Infrastructure Strategy (NCRIS), particularly the National eResearch Collaboration Tools and Resources (NeCTAR) and the Australian National Data Service Projects (ANDS).

The Pan-STARRS1 Surveys (PS1) and the PS1 public science archive have been made possible through contributions by the Institute for Astronomy, the University of Hawaii, the Pan-STARRS

Project Office, the Max-Planck Society and its participating institutes, the Max Planck Institute for Astronomy, Heidelberg and the Max Planck Institute for Extraterrestrial Physics, Garching, The Johns Hopkins University, Durham University, the University of Edinburgh, the Queen's University Belfast, the Harvard-Smithsonian Center for Astrophysics, the Las Cumbres Observatory Global Telescope Network Incorporated, the National Central University of Taiwan, the Space Telescope Science Institute, the National Aeronautics and Space Administration under Grant No. NNX08AR22G issued through the Planetary Science Division of the NASA Science Mission Directorate, the National Science Foundation Grant No. AST-1238877, the University of Maryland, Eotvos Lorand University (ELTE), the Los Alamos National Laboratory, and the Gordon and Betty Moore Foundation.

The VISTA Hemisphere Survey data products served at Astro Data Lab are based on observations collected at the European Organisation for Astronomical Research in the Southern Hemisphere under ESO programme 179.A-2010, and/or data products created thereof.

This publication has made use of data from the VIKING survey from VISTA at the ESO Paranal Observatory, programme ID 179.A-2004. Data processing has been contributed by the VISTA Data Flow System at CASU, Cambridge and WFAU, Edinburgh.

This publication makes use of data products from the Two Micron All Sky Survey, which is a joint project of the University of Massachusetts and the Infrared Processing and Analysis Center/California Institute of Technology, funded by the National Aeronautics and Space Administration and the National Science Foundation.

This publication makes use of data products from the Wide-field Infrared Survey Explorer, which is a joint project of the University of California, Los Angeles, and the Jet Propulsion Laboratory/California Institute of Technology, and NEOWISE, which is a project of the Jet Propulsion Laboratory/California Institute of Technology. WISE and NEOWISE are funded by the National Aeronautics and Space Administration.

Software packages used in this study include Numpy (van der Walt et al. 2011), Scipy (Virtanen et al. 2020), Astropy (Astropy Collaboration et al. 2013), PyeIt (Prochaska et al. 2020), Specutils (Earl et al. 2022), SpectRes (Carnall 2017), and Matplotlib (Hunter 2007).

DATA AVAILABILITY

The data underlying this article will be shared on reasonable request to the corresponding author.

REFERENCES

- Akins H. B., et al., 2023, *ApJ*, **956**, 61
Akiyama M., et al., 2018, *PASJ*, **70**, S34
Aller M. C., Richstone D., 2002, *AJ*, **124**, 3035
Amarantidis S., et al., 2019, *MNRAS*, **485**, 2694
Amaro-Seoane P., et al., 2017, *arXiv e-prints*, p. [arXiv:1702.00786](https://arxiv.org/abs/1702.00786)
Ananna T. T., et al., 2020, *ApJ*, **903**, 85
Ananna T. T., et al., 2022, *ApJS*, **261**, 9
Assef R. J., et al., 2015, *ApJ*, **804**, 27
Astropy Collaboration et al., 2013, *A&A*, **558**, A33
Avni Y., Bahcall J. N., 1980, *ApJ*, **235**, 694
Bañados E., et al., 2018, *Nature*, **553**, 473
Baldry I. K., et al., 2012, *MNRAS*, **421**, 621
Barger A. J., Cowie L. L., Mushotzky R. F., Yang Y., Wang W. H., Steffen A. T., Capak P., 2005, *AJ*, **129**, 578
Bennert V. N., et al., 2021, *ApJ*, **921**, 36
Berti E., Volonteri M., 2008, *ApJ*, **684**, 822
Bhowmick A. K., et al., 2022, *MNRAS*, **516**, 138
Bischetti M., et al., 2017, *A&A*, **598**, A122
Bogdán Á., et al., 2024, *Nature Astronomy*, **8**, 126
Boutsia K., et al., 2020, *ApJS*, **250**, 26
Boutsia K., et al., 2021, *ApJ*, **912**, 111
Boyle B. J., Shanks T., Croom S. M., Smith R. J., Miller L., Loaring N., Heymans C., 2000, *MNRAS*, **317**, 1014
Capellupo D. M., Netzer H., Lira P., Trakhtenbrot B., Mejía-Restrepo J., 2015, *MNRAS*, **446**, 3427
Caplar N., Lilly S. J., Trakhtenbrot B., 2015, *ApJ*, **811**, 148
Carnall A. C., 2017, *arXiv e-prints*, p. [arXiv:1705.05165](https://arxiv.org/abs/1705.05165)
Cen R., Safarzadeh M., 2015, *ApJ*, **798**, L38
Chatterjee K., et al., 2020, *MNRAS*, **499**, 362
Ciotti L., Ostriker J. P., 2001, *ApJ*, **551**, 131
Cisternas M., et al., 2011, *ApJ*, **741**, L11
Coatman L., Hewett P. C., Banerji M., Richards G. T., 2016, *MNRAS*, **461**, 647
Coatman L., Hewett P. C., Banerji M., Richards G. T., Hennawi J. F., Prochaska J. X., 2017, *MNRAS*, **465**, 2120
Costa T., Sijacki D., Trenti M., Haehelm M. G., 2014, *MNRAS*, **439**, 2146
Cristiani S., et al., 2023, *MNRAS*, **522**, 2019
Cutri R. M., et al., 2013, Explanatory Supplement to the AllWISE Data Release Products, Explanatory Supplement to the AllWISE Data Release Products
D'Odorico V., et al., 2023, *MNRAS*, **523**, 1399
Dalla Bontà E., et al., 2020, *ApJ*, **903**, 112
Davidzon I., et al., 2017, *A&A*, **605**, A70
Davies F. B., Hennawi J. F., Eilers A.-C., 2019, *ApJ*, **884**, L19
Davies F. B., Hennawi J. F., Eilers A.-C., 2020, *MNRAS*, **493**, 1330
Davis B. L., Graham A. W., Cameron E., 2019, *ApJ*, **873**, 85
DeGraf C., Sijacki D., 2017, *MNRAS*, **466**, 3331
Devecchi B., Volonteri M., 2009, *ApJ*, **694**, 302
Di Matteo T., Colberg J., Springel V., Hernquist L., Sijacki D., 2008, *ApJ*, **676**, 33
Ding X., et al., 2020, *ApJ*, **888**, 37
Dotti M., Colpi M., Pallini S., Perego A., Volonteri M., 2013, *ApJ*, **762**, 68
Dubois Y., Volonteri M., Silk J., 2014, *MNRAS*, **440**, 1590
Duras F., et al., 2020, *A&A*, **636**, A73
Earl N., et al., 2022, *astropy/specutils*: V1.7.0, doi:[10.5281/zenodo.6207491](https://doi.org/10.5281/zenodo.6207491), <https://doi.org/10.5281/zenodo.6207491>
Edge A., Sutherland W., Kuijken K., Driver S., McMahon R., Eales S., Emerson J. P., 2013, *The Messenger*, **154**, 32
Eilers A.-C., Davies F. B., Hennawi J. F., Prochaska J. X., Lukić Z., Mazzucchelli C., 2017, *ApJ*, **840**, 24
Eilers A.-C., Hennawi J. F., Davies F. B., 2018, *ApJ*, **867**, 30
Eilers A.-C., et al., 2020, *ApJ*, **900**, 37
Eilers A.-C., et al., 2023, *ApJ*, **950**, 68
Fabian A. C., 2012, *ARA&A*, **50**, 455
Fan X., et al., 2006, *AJ*, **132**, 117
Fan X., Bañados E., Simcoe R. A., 2023, *ARA&A*, **61**, 373
Farina E. P., et al., 2022, *ApJ*, **941**, 106
Feng Y., Di Matteo T., Croft R., Khandai N., 2014, *MNRAS*, **440**, 1865
Ferrarese L., Merritt D., 2000, *ApJ*, **539**, L9
Flesch E. W., 2015, *Publ. Astron. Soc. Australia*, **32**, e010
Gebhardt K., et al., 2000, *ApJ*, **539**, L13
Giallongo E., et al., 2019, *ApJ*, **884**, 19
Goulding A. D., et al., 2023, *ApJ*, **955**, L24
Grazian A., et al., 2020, *ApJ*, **897**, 94
Grazian A., et al., 2022, *ApJ*, **924**, 62
Greene J. E., Ho L. C., 2005, *ApJ*, **630**, 122
Greene J. E., et al., 2010, *ApJ*, **721**, 26
Grier C. J., et al., 2019, *ApJ*, **887**, 38
Harikane Y., et al., 2023, *ApJ*, **959**, 39
Håring N., Rix H.-W., 2004, *ApJ*, **604**, L89
Hasinger G., 2008, *A&A*, **490**, 905
He W., et al., 2024, *ApJ*, **962**, 152

- Hoormann J. K., et al., 2019, *MNRAS*, **487**, 3650
- Hopkins P. F., Hernquist L., Cox T. J., Di Matteo T., Martini P., Robertson B., Springel V., 2005, *ApJ*, **630**, 705
- Hopkins P. F., Richards G. T., Hernquist L., 2007, *ApJ*, **654**, 731
- Hunter J. D., 2007, *Computing in Science and Engineering*, **9**, 90
- Inayoshi K., Haiman Z., Ostriker J. P., 2016, *MNRAS*, **459**, 3738
- Inayoshi K., Visbal E., Haiman Z., 2020, *ARA&A*, **58**, 27
- Jiang L., et al., 2016, *ApJ*, **833**, 222
- Kashikawa N., et al., 2015, *ApJ*, **798**, 28
- Kaspi S., Smith P. S., Netzer H., Maoz D., Jannuzi B. T., Giveon U., 2000, *ApJ*, **533**, 631
- Kaspi S., Maoz D., Netzer H., Peterson B. M., Vestergaard M., Jannuzi B. T., 2005, *ApJ*, **629**, 61
- Kaspi S., Brandt W. N., Maoz D., Netzer H., Schneider D. P., Shemmer O., Grier C. J., 2021, *ApJ*, **915**, 129
- Kelly B. C., Merloni A., 2012, *Advances in Astronomy*, **2012**, 970858
- Kelly B. C., Shen Y., 2013, *ApJ*, **764**, 45
- Kelly B. C., Vestergaard M., Fan X., 2009, *ApJ*, **692**, 1388
- Kelly B. C., Vestergaard M., Fan X., Hopkins P., Hernquist L., Siemiginowska A., 2010, *ApJ*, **719**, 1315
- Khrykin I. S., Hennawi J. F., Worseck G., 2019, *MNRAS*, **484**, 3897
- Khrykin I. S., Hennawi J. F., Worseck G., Davies F. B., 2021, *MNRAS*, **505**, 649
- King A. R., Pringle J. E., 2006, *MNRAS*, **373**, L90
- King A. R., Lubow S. H., Ogilvie G. I., Pringle J. E., 2005, *MNRAS*, **363**, 49
- King A. R., Pringle J. E., Hofmann J. A., 2008, *MNRAS*, **385**, 1621
- Kollmeier J. A., et al., 2006, *ApJ*, **648**, 128
- Kormendy J., Ho L. C., 2013, *ARA&A*, **51**, 511
- Kormendy J., Richstone D., 1995, *ARA&A*, **33**, 581
- Kormendy J., Bender R., Cornell M. E., 2011, *Nature*, **469**, 374
- Kulier A., Ostriker J. P., Natarajan P., Lackner C. N., Cen R., 2015, *ApJ*, **799**, 178
- Lai S., Onken C. A., Wolf C., Bian F., Cupani G., Lopez S., D'Odorico V., 2023, *MNRAS*, **526**, 3230
- Lai S., Onken C. A., Wolf C., Bian F., Fan X., 2024, *MNRAS*, **527**, 3912
- Larson R. L., et al., 2023, *ApJ*, **953**, L29
- Lawrence A., 1991, *MNRAS*, **252**, 586
- Lawrence A., Elvis M., 2010, *ApJ*, **714**, 561
- Li Y., et al., 2007, *ApJ*, **665**, 187
- Li W., Inayoshi K., Onoue M., Toyouchi D., 2023, *ApJ*, **950**, 85
- Li J., et al., 2024, *arXiv e-prints*, p. arXiv:2403.00074
- Lira P., et al., 2018, *ApJ*, **865**, 56
- Lodato G., Pringle J. E., 2006, *MNRAS*, **368**, 1196
- Loeb A., Rasio F. A., 1994, *ApJ*, **432**, 52
- López S., et al., 2016, *A&A*, **594**, A91
- Lupi A., Haardt F., Dotti M., Fiacconi D., Mayer L., Madau P., 2016, *MNRAS*, **456**, 2993
- Madau P., Rees M. J., 2001, *ApJ*, **551**, L27
- Madau P., Haardt F., Dotti M., 2014, *ApJ*, **784**, L38
- Magorrian J., et al., 1998, *AJ*, **115**, 2285
- Maiolino R., et al., 2023, *arXiv e-prints*, p. arXiv:2308.01230
- Marconi A., Hunt L. K., 2003, *ApJ*, **589**, L21
- Marocco F., et al., 2021, *ApJS*, **253**, 8
- Martin G., et al., 2018, *MNRAS*, **476**, 2801
- Matsuoka Y., et al., 2016, *ApJ*, **828**, 26
- Matsuoka Y., et al., 2018, *ApJ*, **869**, 150
- Matsuoka Y., et al., 2023, *ApJ*, **949**, L42
- Matthee J., et al., 2024, *ApJ*, **963**, 129
- Mazzucchelli C., et al., 2023, *A&A*, **676**, A71
- McGreer I. D., Fan X., Jiang L., Cai Z., 2018, *AJ*, **155**, 131
- McLure R. J., Dunlop J. S., 2004, *MNRAS*, **352**, 1390
- McMahon R. G., Banerji M., Gonzalez E., Koposov S. E., Bejar V. J., Lodieu N., Rebolo R., VHS Collaboration 2013, *The Messenger*, **154**, 35
- Mejía-Restrepo J. E., Trakhtenbrot B., Lira P., Netzer H., Capellupo D. M., 2016, *MNRAS*, **460**, 187
- Mejía-Restrepo J. E., Trakhtenbrot B., Lira P., Netzer H., 2018, *MNRAS*, **478**, 1929
- Merloni A., et al., 2014, *MNRAS*, **437**, 3550
- Merritt D., Ferrarese L., 2001, *MNRAS*, **320**, L30
- Morey K. A., Eilers A.-C., Davies F. B., Hennawi J. F., Simcoe R. A., 2021, *ApJ*, **921**, 88
- Mortlock D. J., et al., 2011, *Nature*, **474**, 616
- Netzer H., 2019, *MNRAS*, **488**, 5185
- Ni Y., Di Matteo T., Gilli R., Croft R. A. C., Feng Y., Norman C., 2020, *MNRAS*, **495**, 2135
- Niida M., et al., 2020, *ApJ*, **904**, 89
- Novak G. S., Ostriker J. P., Ciotti L., 2011, *ApJ*, **737**, 26
- Ohsuga K., Mineshige S., Mori M., Umemura M., 2002, *ApJ*, **574**, 315
- Onken C. A., et al., 2019, *Publ. Astron. Soc. Australia*, **36**, e033
- Onken C. A., Wolf C., Bian F., Fan X., Hon W. J., Raitheal D., Tisserand P., Lai S., 2022, *MNRAS*, **511**, 572
- Oppenheimer B. D., Schaye J., 2013, *MNRAS*, **434**, 1063
- Pacucci F., Loeb A., 2024, *ApJ*, **964**, 154
- Page M. J., Carrera F. J., 2000, *MNRAS*, **311**, 433
- Park D., Barth A. J., Woo J.-H., Malkan M. A., Treu T., Bennert V. N., Assef R. J., Pancoast A., 2017, *ApJ*, **839**, 93
- Peng C. Y., Impey C. D., Ho L. C., Barton E. J., Rix H.-W., 2006, *ApJ*, **640**, 114
- Piana O., Dayal P., Volonteri M., Choudhury T. R., 2021, *MNRAS*, **500**, 2146
- Porciani C., Norberg P., 2006, *MNRAS*, **371**, 1824
- Porciani C., Magliocchetti M., Norberg P., 2004, *MNRAS*, **355**, 1010
- Portegies Zwart S. F., Baumgardt H., Hut P., Makino J., McMillan S. L. W., 2004, *Nature*, **428**, 724
- Prochaska J., et al., 2020, *The Journal of Open Source Software*, **5**, 2308
- Proga D., Stone J. M., Kallman T. R., 2000, *ApJ*, **543**, 686
- Punturo M., et al., 2010, *Classical and Quantum Gravity*, **27**, 194002
- Rakshit S., Stalin C. S., Kotilainen J., 2020, *ApJS*, **249**, 17
- Rees M. J., 1984, *ARA&A*, **22**, 471
- Regan J. A., Haehnelt M. G., 2009, *MNRAS*, **396**, 343
- Reines A. E., Volonteri M., 2015, *ApJ*, **813**, 82
- Reitze D., et al., 2019, in *Bulletin of the American Astronomical Society*, p. 35 (arXiv:1907.04833), doi:10.48550/arXiv.1907.04833
- Reynolds C. S., 2019, *Nature Astronomy*, **3**, 41
- Reynolds C. S., 2021, *ARA&A*, **59**, 117
- Richards G. T., et al., 2006, *ApJS*, **166**, 470
- Richards G. T., et al., 2011, *AJ*, **141**, 167
- Runnoe J. C., Brotherton M. S., Shang Z., 2012, *MNRAS*, **427**, 1800
- Runnoe J. C., Brotherton M. S., Shang Z., DiPompeo M. A., 2013, *MNRAS*, **434**, 848
- Salpeter E. E., 1964, *ApJ*, **140**, 796
- Santos S., et al., 2021, *MNRAS*, **505**, 1117
- Saturni F. G., et al., 2018, *A&A*, **617**, A118
- Satyavolu S., Kulkarni G., Keating L. C., Haehnelt M. G., 2023a, *MNRAS*, **521**, 3108
- Satyavolu S., et al., 2023b, *MNRAS*, **522**, 4918
- Schawinski K., Koss M., Berney S., Sartori L. F., 2015, *MNRAS*, **451**, 2517
- Schindler J.-T., Fan X., McGreer I. D., Yang Q., Wu J., Jiang L., Green R., 2017, *ApJ*, **851**, 13
- Schindler J.-T., et al., 2019a, *ApJS*, **243**, 5
- Schindler J.-T., et al., 2019b, *ApJ*, **871**, 258
- Schindler J.-T., et al., 2023, *ApJ*, **943**, 67
- Schmidt M., 1968, *ApJ*, **151**, 393
- Schneider R., Valiante R., Trinca A., Graziani L., Volonteri M., Maiolino R., 2023, *MNRAS*, **526**, 3250
- Schulze A., Wisotzki L., 2010, *A&A*, **516**, A87
- Schulze A., et al., 2015, *MNRAS*, **447**, 2085
- Selsing J., Fynbo J. P. U., Christensen L., Krogager J. K., 2016, *A&A*, **585**, A87
- Seth A., Agüeros M., Lee D., Basu-Zych A., 2008, *ApJ*, **678**, 116
- Shankar F., Weinberg D. H., Miralda-Escudé J., 2009, *ApJ*, **690**, 20
- Shankar F., Crocce M., Miralda-Escudé J., Fosalba P., Weinberg D. H., 2010, *ApJ*, **718**, 231
- Shankar F., Weinberg D. H., Miralda-Escudé J., 2013, *MNRAS*, **428**, 421
- Shen Y., 2013, *Bulletin of the Astronomical Society of India*, **41**, 61
- Shen Y., Kelly B. C., 2012, *ApJ*, **746**, 169
- Shen Y., Liu X., 2012, *ApJ*, **753**, 125

- Shen Y., et al., 2007, *AJ*, 133, 2222
- Shen Y., et al., 2009, *ApJ*, 697, 1656
- Shen Y., et al., 2011, *ApJS*, 194, 45
- Shen Y., et al., 2019, *ApJ*, 873, 35
- Shields G. A., 1978, *Nature*, 272, 706
- Sijacki D., Springel V., Haehnelt M. G., 2009, *MNRAS*, 400, 100
- Sijacki D., Vogelsberger M., Genel S., Springel V., Torrey P., Snyder G. F., Nelson D., Hernquist L., 2015, *MNRAS*, 452, 575
- Silk J., Begelman M. C., Norman C., Nusser A., Wyse R. F. G., 2024, *ApJ*, 961, L39
- Skrutskie M. F., et al., 2006, *AJ*, 131, 1163
- Smethurst R. J., et al., 2023, *MNRAS*,
- Smidt J., Whalen D. J., Johnson J. L., Surace M., Li H., 2018, *ApJ*, 865, 126
- Soltan A., 1982, *MNRAS*, 200, 115
- Trakhtenbrot B., 2014, *ApJ*, 789, L9
- Trakhtenbrot B., Netzer H., 2012, *MNRAS*, 427, 3081
- Trakhtenbrot B., Netzer H., Lira P., Shemmer O., 2011, *ApJ*, 730, 7
- Trakhtenbrot B., Volonteri M., Natarajan P., 2017, *ApJ*, 836, L1
- Tucci M., Volonteri M., 2017, *A&A*, 600, A64
- Übler H., et al., 2023, *A&A*, 677, A145
- Ueda Y., Akiyama M., Ohta K., Miyaji T., 2003, *ApJ*, 598, 886
- Ueda Y., Akiyama M., Hasinger G., Miyaji T., Watson M. G., 2014, *ApJ*, 786, 104
- Valentini M., Gallerani S., Ferrara A., 2021, *MNRAS*, 507, 1
- Valiante R., Schneider R., Volonteri M., Omukai K., 2016, *MNRAS*, 457, 3356
- Vasudevan R. V., Fabian A. C., 2007, *MNRAS*, 381, 1235
- Vasudevan R. V., Mushotzky R. F., Winter L. M., Fabian A. C., 2009, *MNRAS*, 399, 1553
- Vasudevan R. V., Fabian A. C., Reynolds C. S., Aird J., Dauser T., Gallo L. C., 2016, *MNRAS*, 458, 2012
- Vestergaard M., Osmer P. S., 2009, *ApJ*, 699, 800
- Vestergaard M., Peterson B. M., 2006, *ApJ*, 641, 689
- Vijarnwannaluk B., et al., 2022, *ApJ*, 941, 97
- Virtanen P., et al., 2020, *Nature Methods*, 17, 261
- Volonteri M., Bellovary J., 2012, *Reports on Progress in Physics*, 75, 124901
- Volonteri M., Haardt F., Madau P., 2003, *ApJ*, 582, 559
- Volonteri M., Sikora M., Lasota J. P., Merloni A., 2013, *ApJ*, 775, 94
- Volonteri M., Dubois Y., Pichon C., Devriendt J., 2016, *MNRAS*, 460, 2979
- Volonteri M., Habouzit M., Colpi M., 2021, *Nature Reviews Physics*, 3, 732
- Wang F., et al., 2018, *ApJ*, 869, L9
- Wang F., et al., 2021, *ApJ*, 907, L1
- White M., Martini P., Cohn J. D., 2008, *MNRAS*, 390, 1179
- Willott C. J., Rawlings S., Blundell K. M., Lacy M., 2000, *MNRAS*, 316, 449
- Willott C. J., et al., 2010a, *AJ*, 139, 906
- Willott C. J., et al., 2010b, *AJ*, 140, 546
- Wise J. H., Turk M. J., Abel T., 2008, *ApJ*, 682, 745
- Wolf C., et al., 2018, *Publ. Astron. Soc. Australia*, 35, e010
- Wright E. L., et al., 2010, *AJ*, 140, 1868
- Wu Q., Shen Y., 2022, *ApJS*, 263, 42
- Wu J., et al., 2022, *MNRAS*, 517, 2659
- Wyithe J. S. B., Loeb A., 2012, *MNRAS*, 425, 2892
- Yang J., et al., 2016, *ApJ*, 829, 33
- Yang J., et al., 2019, *AJ*, 157, 236
- Yang J., et al., 2020, *ApJ*, 897, L14
- Yang G., et al., 2023, *ApJ*, 950, L5
- Yu Q., Tremaine S., 2002, *MNRAS*, 335, 965
- Zhu Q., Li Y., Li Y., Maji M., Yajima H., Schneider R., Hernquist L., 2022, *MNRAS*, 514, 5583
- Zubovas K., King A., 2021, *MNRAS*, 501, 4289
- van der Walt S., Colbert S. C., Varoquaux G., 2011, *Computing in Science and Engineering*, 13, 22

This paper has been typeset from a $\text{\TeX}/\text{\LaTeX}$ file prepared by the author.